Lawrence Berkeley National Laboratory

Title
First-principles calculations and experimental studies of XYZ 2 thermoelectric compounds: detailed analysis of van der Waals interactions

Authors
Pöhls, Jan-Hendrik
Luo, Zhe
Aydemir, Umut
et al.

First-principles calculations and experimental studies of XYZ_2 thermoelectric compounds: detailed analysis of van der Waals interactions†

Jan-Hendrik Pöhls,[a] Zhe Luo, [iD][bc] Umut Aydemir,[cd] Jon-Paul Sun,[ae] Shiqiang Hao,[c] Jiangang He,[c] Ian G. Hill,[af] Geoffroy Hautier, [iD][g] Anubhav Jain,[h] Xiaoqin Zeng,[b] Chris Wolverton,[c] G. Jeffrey Snyder, [iD][c] Hong Zhu[ij] and Mary Anne White [iD] *[afk]

First-principles calculations can accelerate the search for novel high-performance thermoelectric materials. However, the prediction of the thermoelectric properties is strongly dependent on the approximations used for the calculations. Here, thermoelectric properties were calculated with different computational approximations (*i.e.*, PBE-GGA, HSE06, spin−orbit coupling and DFT-D3) for three layered XYZ_2 compounds ($TmAgTe_2$, $YAgTe_2$, and $YCuTe_2$). In addition to the computations, the structural, electrical and thermal properties of these compounds were measured experimentally and compared to the computations. An enhanced prediction of the crystal structure and heat capacity was achieved with the inclusion of van der Waals interactions due to more accurate modeling of the interatomic forces. In particular, a large shift of the acoustic phonons and low-frequency optical phonons to lower frequencies was observed from the dispersion-optimized structure. From the phonon dispersion curves of these compounds, the ultralow thermal conductivity in the investigated XYZ_2 compounds could be described by a recent developed minimum thermal conductivity model. For the prediction of the electrical conductivity, a temperature-dependent relaxation time was used, and it was limited by acoustic phonons. While HSE06 has only a small influence on the electrical properties due to a computed band gap energy of >0.25 eV, the inclusion of both van der Waals interactions and spin−orbit coupling leads to a more accurate band structure, resulting in better prediction of electrical properties. Furthermore, the experimental thermoelectric properties of $YAgTe_2$, $TmAg_{0.95}Zn_{0.05}Te_2$ and $TmAg_{0.95}Mg_{0.05}Te_2$ were measured, showing an increase in zT of $TmAg_{0.95}Zn_{0.05}Te_2$ by more than 35% ($zT = 0.47 \pm 0.12$) compared to $TmAgTe_2$.

[a]*Department of Physics and Atmospheric Science, Dalhousie University, Halifax, NS B3H 4R2, Canada. E-mail: mawhite@dal.ca*

[b]*National Engineering Research Center of Light Alloy Net Forming, Shanghai Jiao Tong University, Shanghai 200240, People's Republic of China*

[c]*Department of Materials Science and Engineering, Northwestern University, IL 60208, USA*

[d]*Department of Chemistry, Koc University, Sariyer, Istanbul 34450, Turkey*

[e]*Department of Mechanical Engineering and Materials Science, Duke University, Durham, NC 27708, USA*

[f]*Clean Technologies Research Institute, Dalhousie University, Halifax, NS B3H 4R2, Canada*

[g]*Institute of Condensed Matter and Nanosciences (IMCN), Université Catholique de Louvain, Chemin des Étoiles 8, B-1348 Louvain-la-Neuve, Belgium*

[h]*Energy Technologies Area, Lawrence Berkeley National Lab, 1 Cyclotron Rd, Berkeley, CA, USA*

[i]*State Key Laboratory of Metal Matrix Composite, Shanghai Jiao Tong University, Shanghai 200240, People's Republic of China*

[j]*University of Michigan – Shanghai Jiao Tong University Joint Institute, Shanghai Jiao Tong University, Shanghai 200240, People's Republic of China*

[k]*Department of Chemistry, Dalhousie University, Halifax, NS B3H 4R2, Canada*

1. Introduction

In recent years, first-principles calculations (*e.g.*, based on density functional theory [DFT]) have become a common technique to compute diverse properties, such as crystal structures,[1,2] optical properties,[3,4] and electrical[5,6] and thermal conductivity.[7,8] With the exponential growth in computing power and the advanced theoretical understanding, first-principles calculations have been demonstrated to accelerate the search for new functional compounds and contribute to the optimization of the materials' properties for solar cells,[9] photocatalysts,[10] and batteries.[11–13]

First-principles calculations can be particularly beneficial in thermoelectric materials research because the discovery of new high-performance thermoelectrics is challenging due to the strong interdependence of the electrical and thermal properties. The performance of thermoelectric materials is related to the thermoelectric figure of merit, zT,

$$zT = \frac{S^2 T}{\rho(\kappa_e + \kappa_p)} \quad (1)$$

where S is the Seebeck coefficient, ρ is the electrical resistivity, T is the absolute temperature and the thermal conductivity is separated into electronic, κ_e, and phononic, κ_p, contributions. The electronic properties (ρ, S, and κ_e) are strongly dependent on the carrier concentration and band structure, whereas ρ and κ_p can be influenced by the phonon dispersion curves and defects such as grain boundaries.[14] Insight into the electronic and thermal properties can be provided by first-principles calculations. Several computational studies have been performed on thermoelectric classes of materials, including half-[15] and full Heusler alloys,[16] sulfides,[17] zinc antimonides,[18,19] and metal phosphides.[20] In a previous high-throughput screening of 9000 inorganic compounds within The Materials Project (http://www.materialsproject.org),[21] we have revealed a new class of high-performance thermoelectric materials, namely XYZ_2 (X,Y: rare earth or transition metals, Z: group VI element).[22] In the screening, the electronic properties were computed from PBE-GGA band structures using Boltzmann transport equations and the relaxation time was set to 10^{-14} s. The phononic contribution to the thermal conductivity was set to 0.5 W m^{-1} K^{-1} and more than 500 XYZ_2 compounds revealed high computed thermoelectric performance. Based on this high-throughput screening, the experimental thermoelectric properties of two XYZ_2 compounds, TmAgTe$_2$ (ref. 22) and YCuTe$_2$,[23] were shown to have potential for high-performance thermoelectrics due to multiple band degeneracies. While YCuTe$_2$ has a relatively high experimental zT of 0.73 at 780 K,[23] the experimental thermoelectric performance of TmAgTe$_2$ is limited by a low carrier concentration. According to defect calculations, the low carrier concentration is a result of Tm$_{Ag}$ anti-site defects (i.e., trivalent Tm occupying monovalent Ag sites).[22] In a separate study, Lin et al. investigated the thermoelectric properties of TmCuTe$_2$ and found a maximum zT of 0.81 at 745 K,[24] similar to YCuTe$_2$. Although the experimental results are promising, the computed thermoelectric performance exceeded the measured values, and to advance predictive studies it is desirable to delineate the origins of the overestimation in this class of potential high-performance thermoelectric materials.

The computed electronic properties are strongly dependent on the accuracies of the electronic band structures and the relaxation time. The latter is challenging to compute in high-throughput studies due to the high computing cost of electron–phonon coupling calculations and is in general set to a constant value (e.g., $\tau = 10^{-14}$ s).[22,25] However, the relaxation time is strongly dependent on the temperature, resulting in a dramatic shortening of the relaxation time at high temperature due to electron–phonon interactions. Several approximations are currently used to calculate the electronic band structures. Whereas the local density approximation (LDA) and the generalized gradient approximation (GGA) underestimate the band gap energy, the Heyd–Scuseria–Ernzerhof (HSE06) screened-hybrid functional generally leads to a more accurate estimation of the band gap energy than semi-local DFT-functionals.[26]

The mean errors in band gap energies of various hybrid functionals were compared and the lowest mean error was found for HSE06 ($\varepsilon = -0.24$ eV compared to experiments).[27] That study revealed that HSE06 tends to underestimate the band gap energy, in particular for large band gap semiconductors. Similar results were reported by Chan and Ceder who found a mean absolute error of 0.24 eV, however, the error increases for transition-metal compounds ($\varepsilon = 0.41$ eV).[28] They also compared the semi-local GGA functional to experiments leading to a greater underestimation of the computed band gap energy ($\varepsilon = 0.73$ eV). For large band-gap semiconductors, Setyawan et al. reported a relative uncertainty of $\sim$42% between the computed band gaps using PBE-GGA and experimental values.[29] In addition to the exchange–correlation functionals, various corrections can influence the electronic band structures. For instance, if the compound contains heavy elements, spin–orbit coupling (SOC) splits the degenerate bands at the band edges due to the difference in band effective masses. A decrease in degeneracy leads, in general, to a reduction of the band gap energy and the desired electronic properties. Zhu et al. reported a dramatical reduction of the p-type power factor of HT-TmAgTe$_2$ with the inclusion of the SOC due to a split of the light-hole and heavy-hole bands at the valence band maximum.[22] The computed power factor decreased nearly by 1/3 compared to the power factor without SOC.

One approach that is rarely discussed in the literature is the inclusion of dispersion-corrected crystal structures to predict the electronic band structure. Dybala et al. compared the energy difference between experimental optical transitions and the computed values in transition metal chalcogenides, showing that DFT-D3 not only enhanced the prediction of the crystal structure in layered transition metal dichalcogenides but also improved the prediction of the pressure dependence to the electronic band structure.[30] Furthermore, the prediction of the stability and lithiation voltage in layered lithium cobalt oxides can be enhanced with the inclusion of van der Waals interactions.[31] In addition to the electronic/optical properties, the phonon dispersion curves of graphite were compared using different dispersion corrections and a dramatic increase of accuracy was observed with the inclusion of DFT-D3 compared to solely PBE-GGA.[32] In one of the few thermoelectric studies including van der Waals interactions, the calculated electronic band structure of Bi$_2$Te$_3$ and Bi$_2$Se$_3$ gave significantly improved prediction of the bands.[33] These studies revealed that the inclusion of van der Waals interactions is crucial for accurate prediction of the physical properties in layered materials, such as XYZ_2 compounds and other layered materials.[34–36] Furthermore, the electronic band structure depends on the temperature, as previously discussed by van Setten et al.[37] While this temperature effect can change the electronic band structure and hence, the predicted electronic properties, it is beyond the scope of the present study.

In the present study, the thermoelectric properties of TmAgTe$_2$, YAgTe$_2$, and YCuTe$_2$ were investigated in computational and experimental studies. We determined the crystal structure, the electronic and thermal properties with and without inclusion of dispersion forces for the low-temperature

phases of TmAgTe$_2$ and YAgTe$_2$, and compared them with experiments. The inclusion of van der Waals interactions not only enhanced the prediction of the lattice parameters and heat capacity by accurately computing the interatomic forces, but also reduced the band gap energy and pushed the Te–Tm–Ag valence bands near the valence band maximum downwards. In addition to the van der Waals interactions, spin–orbit coupling also reduces the degeneracy of the valence bands by splitting the light-hole and heavy-hole Te–Tm–Ag bands. For the calculation of the electrical resistivity, a temperature-dependent relaxation time limited by acoustic phonons was implemented especially enhancing the prediction of the high-temperature resistivity. Both the inclusion of spin–orbit coupling and dispersion forces improved the prediction of the calculated electronic properties compared to the PBE-GGA properties, whereas the calculation using the HSE06 exchange functional did not improve the electronic properties due to an overestimation of the band gap energy. All studied XYZ_2 compounds exhibit ultralow thermal conductivity (*i.e.*, lower experimental thermal conductivity than the predicted amorphous limit)[38,39] which can be described by a recent developed thermal conductivity model where the phonon mean free path is limited by two-phonon processes.[20,40] In addition to the comparison between computation and experiments, the experimental thermoelectric properties of YAgTe$_2$ was measured leading to low zT due to a low electron mobility. Furthermore, we doped TmAgTe$_2$ on the Ag-site with Mg and Zn, which led to significantly enhanced thermoelectric properties.

2. Computational and experimental details

2.1. Electronic band structure and phonon dispersion calculations

First-principles calculations were performed using the Vienna Ab initio Simulation Package (VASP)[41] with the Perdew–Burke–Ernzerhof (PBE) generalized gradient approximation (GGA)[42] and the projected augmented (PAW) pseudopotentials[43] with an energy cutoff of 520 eV for the plane-wave basis. The possibility of f-electrons in Tm near the valence band or within band gap in TmAgTe$_2$ was ruled out, as previously discussed by Zhu *et al.*[22] As result, we implemented the same pseudopotential in which the valence of Tm were set to 3 (Tm_3; f-electrons are in the core). Electron occupation was smeared using a Gaussian smearing during structure optimization and band structure calculation. For an improved prediction of the band gap energy, the electronic band structures also were computed with the screened hybrid functional HSE06.[44,45] For the low-temperature phase of TmAgTe$_2$ (LT-TmAgTe$_2$) and LT-YAgTe$_2$ with layered structures, the DFT-D3 method with zero damping[46] was adopted in the calculations to include van der Waals interactions. The electronic transport properties were computed using the BoltzTraP code.[47] For the calculation of ρ and κ_e, a temperature-dependent relaxation time was applied where the relaxation time is limited by acoustic phonons. The Fermi surfaces were analyzed with the XCrySDen package.[48]

The phonon dispersion curves were calculated with the frozen phonon methods implemented in the Phonopy package[49] using supercells of 288 atoms for LT-TmAgTe$_2$ and LT-YAgTe$_2$, 300 atoms for HT-TmAgTe$_2$. The thermal expansion of LT-TmAgTe$_2$ and LT-YAgTe$_2$ was calculated with the quasi-harmonic approximation[50] using a smaller supercell containing 96 atoms. Although small imaginary frequencies were observed at Γ point in the 96-atom supercell (they disappear in larger supercells, *i.e.*, $\sim$288 atom supercell), the difference in Helmholtz free energy of phonons between the small and large supercell is negligible ($\sim$10^{-4} eV per atom). Since LT-YCuTe$_2$ is disordered, we approximated the primitive cell using an ordered structure with the lowest energy among the considered structures (see detailed information in the ESI). A supercell with 128 atoms was used in the phonon calculation for LT-YCuTe$_2$. The lattice constants were obtained from experiments[23] and were fixed during structure optimization while the positions of atoms were allowed to relax. Fitted lattice constants of approximated LT-YCuTe$_2$ with Birch–Murnaghan equation of states varied from original experimental values by less than 0.5%.

2.2. Sample preparation

For the synthesis of TmAgTe$_2$, TmAg$_{0.95}$Mg$_{0.05}$Te$_2$, TmAg$_{0.95}$Zn$_{0.05}$Te$_2$, YAgTe$_2$, and YCuTe$_2$ stoichiometric amounts of Tm pieces (99.9% purity, metal basis, Alfa Aesar), Ag pieces (99.999% purity, metals basis, Alfa Aesar), Mg slug (99.95% purity, metal basis, Alfa Aesar), Zn shot (99.999% purity, metal basis, Alfa Aesar), Te pieces (99.999% purity, metal basis, Alfa Aesar), Y pieces (99.9% purity, metal basis, Alfa Aesar), and Cu slug (99.995% purity, oxygen was removed using a reduction furnace with a continuous flow of Ar with 2% H$_2$ at $\sim$950 K, Alfa Aesar) with a total mass of 3.5 g were sealed in a silica ampoule under high vacuum ($\sim$10^{-6} mbar). For the synthesis of YCuTe$_2$, the silica tubes were additionally carbon-coated. In addition to the YAgTe$_2$ and YCuTe$_2$ as parent compounds, intrinsically doped compounds (Y$_{0.98}$Ag$_{1.02}$Te$_{1.98}$ and Y$_{0.96}$Cu$_{1.08}$Te$_2$) were synthesized.

All ampoules were heated in a vertical tube furnace and the temperature profiles were modified depending on the composition. As previously reported,[22] the ampoules of the parent TmAgTe$_2$ and extrinsically doped compounds were heated to 1443 K in 30 h and annealed at that temperature for 15 h. The ampoules were slowly cooled to 873 K over 30 h and annealed at that temperature for a week, followed by quenching in water to room temperature. The ampoules of the YAgTe$_2$ and the intrinsically doped compounds were heated to 1443 K in 40 h, annealed at that temperature for 15 h, slowly cooled to 473 K over 45 h and then cooled with the furnace. The same temperature profile as reported by Aydemir *et al.* was used for YCuTe$_2$.[23] The ampoules were first heated to 648 K over 10 h, followed to 1073 K over 15 h, and eventually 1443 K over 15 h. At that temperature the sample was annealed for 15 h, and then slowly cooled to 1073 K over 15 h, to 673 K over 15 h and finally to 373 K over 15 h. The furnace was then turned off and the samples were cooled in the furnace. (Note that the carbon coating was removed in the high-temperature treatment.)

All resulting ingots were hand-ground to a fine powder and ~1.5 g of the powder was filled in a 1.27 cm in diameter high-density graphite die (POCO). The parent and extrinsically doped $TmAgTe_2$ powders were sintered in a rapid hot press using RF induction heating at 973 K under a pressure of 40 MPa for one hour and cooled to room temperature over two hours. $YAgTe_2$ and $YCuTe_2$ powders were sintered at 873 K under a pressure of 80 MPa. While $YCuTe_2$ was cooled to room temperature over two hours, $YAgTe_2$ was additionally annealed at 673 K for one hour and then cooled to room temperature over two hours. All sample preparations were handled in an argon-filled glovebox to avoid oxidization of the elements.

2.3. Sample characterization

X-ray diffraction (XRD) was performed using a PANalytical X'Pert Pro diffractometer (45 kV, 40 mA, Cu-Kα radiation) with reflection mode. The lattice parameters were refined with the LeBail method using the software Rietica.

Potential phase transitions were determined using a TA Instruments™ Q200 differential scanning calorimeter (DSC) that had been calibrated with In (99+%, $m = 5.12 \pm 0.01$ mg). The samples ($m = 7$–13 mg, hot-pressed pellets) were hermetically sealed in aluminum pans and the thermograms were recorded at a scanning rate of 10 K min⁻¹.

Low-temperature heat capacity was measured from 0.4 K to 300 K using a thermal-relaxation micro-calorimetry in a Physical Properties Measurement System (PPMS, Quantum Design) under high vacuum (<10⁻⁴ torr). More information about the relaxation technique for both ⁴He and ³He measurements can be found in ref. 51. High-temperature heat capacity ($T > 320$ K) was measured via the enthalpic method in the same DSC described above. Three measurements were performed in which intervals of 10 K were recorded with constant scanning rates of 2 K min⁻¹ under N_2 atmosphere. Before and after each temperature step, the calorimeter was held isothermally for 5 min. Three experiments were performed (empty Al pan with mass m_0, high-purity sapphire as a standard sample with mass $m_{sapphire}$, and the sample with mass m_{sample}). The sapphire and the sample were hermetically sealed in aluminum pans with masses $m_{Al,sapphire}$ and $m_{Al,sample}$, respectively, and the heat flow, $\dot{Q}$, of the sapphire, $\delta\dot{Q}_{sapphire}$, and sample, $\delta\dot{Q}_{sample}$, were calculated by

$$\delta\dot{Q}_{sapphire} = \delta\dot{Q}_{Al,sapphire} - \frac{m_{Al,sapphire}}{m_0}\delta\dot{Q}_0 \qquad (2)$$

and

$$\delta\dot{Q}_{sample} = \delta\dot{Q}_{Al,sample} - \frac{m_{Al,sample}}{m_0}\delta\dot{Q}_0 \qquad (3)$$

respectively, where $\delta\dot{Q}_0$ is the heat flow of the empty Al pan. The heat flows were integrated over time (F) and the heat capacity was scaled to the heat capacity of sapphire:

$$C_{p,sample} = \frac{F_{sample}}{F_{sapphire}}\frac{m_{sapphire}}{m_{sample}}C_{p,sapphire} \qquad (4)$$

where the heat capacity of sapphire, $C_{p,sapphire}$, was taken from ref. 52.

The thermal expansion properties of XYZ_2 compounds (thickness = 0.9–1.4 mm) were determined using a Netzsch dilatometer (DIL 402C) and a scanning rate of 5 K min⁻¹ under vacuum. Prior the measurements, the dilatometer was calibrated with silica samples of thickness similar to the actual sample.

Raman spectra were recorded at room temperature using a Jobin-Yvon T64000 Micro Raman Triple Grating spectrometer. The micro-Raman spectrometer is equipped with an argon laser ($\lambda_{Ar} = 632.8$ nm) and open electrode CCD detector.

The experimental DOS was acquired using ultraviolet photoelectron spectroscopy (UPS) below the Fermi energy and inverse photoemission spectroscopy (IPES) above the Fermi energy. UPS measurements were performed with a He discharge lamp which has two energies, 21.22 eV for He I and 40.81 eV for He II. Prior the measurements, the samples were sputtered with Ar ions to remove surface contamination and oxidation. More information about UPS and IPES measurements can be found in ref. 53.

2.4. Transport properties measurements

The electrical resistivity and Hall coefficient measurements were performed using the van der Pauw technique in a magnetic field of 2 T using pressure-assisted tungsten electrodes in the temperature range from 300 K up to 875 K.[54] The Seebeck coefficients were acquired using chromel–Nb thermocouples by applying an oscillated temperature gradient of ±7.5 K above 300 K.[55] High-temperature thermal conductivity was calculated from the measured thermal diffusivity, D, the mass density, ρ, and the experimental heat capacity at constant pressure, C_p ($\kappa = D\rho C_p$). The thermal diffusivity was measured using a Netzsch LFA 457 laser flash apparatus and the density of the samples was measured using Archimedes' principle.

Below 300 K, the Seebeck coefficient and thermal conductivity were determined using a PPMS (op. cit.) and the thermal transport option (TTO) under high vacuum. The samples were adhered between two gold-plated copper disks with silver epoxy (Tra-Bond 2902) and fixed on the thermal transport stage.[20] The Seebeck coefficient was measured from a voltage drop by applying a temperature gradient. The thermal conductivity was determined from the thermal conductance and the sample geometry.[56,57] Blackbody radiation was corrected using an emissivity of one.

3. Results and discussion

3.1. Characterization

All three parent compounds, $TmAgTe_2$, $YAgTe_2$, and $YCuTe_2$, display at least two polymorphs, a low-temperature (LT) phase and a high-temperature (HT) phase, as shown in Fig. 1.

At low temperature, both $TmAgTe_2$ and $YAgTe_2$ crystallize in the tetragonal phase with space group $P\bar{4}2_1m$ (Fig. 1(a) and (c)) which transforms at high temperature to the trigonal phases with space group $P\bar{3}m1$ (Fig. 1(b)) and $P\bar{3}$ (Fig. 1(d)) for $TmAgTe_2$ and $YAgTe_2$, respectively. Based on the computational study, both LT phases are composed of a mixture of distorted $TmTe_6$

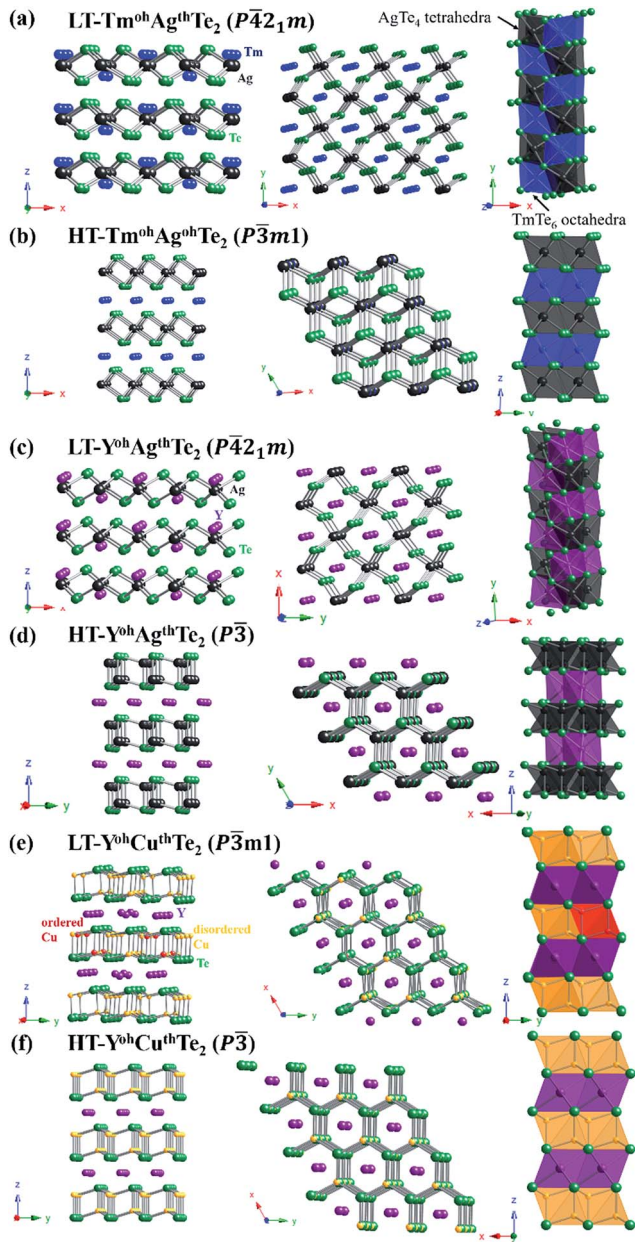**Fig. 1** Crystal structures of (a) the LT phase ($P\bar{4}2_1m$) and (b) the HT phase ($P\bar{3}m1$) of TmAgTe$_2$, (c) the LT phase ($P\bar{4}2_1m$) and (d) the HT phase ($P\bar{3}$) of YAgTe$_2$, and (e) the LT phase ($P\bar{3}m1$) and (f) the HT phase ($P\bar{3}$) of YCuTe$_2$ (oh = octahedral interstices, th = tetrahedral interstices).

(YTe$_6$) octahedra (Tm^{oh} (Y^{oh})) [oh: octahedral interstices, and th: tetrahedral interstices] and AgTe$_4$ tetrahedra (Agth) and forms a ladder-like structure in which Tm (Y) fills the large channels. In the HT phases, Tm (Y) and Ag occupy octahedral interstices, Tm^{oh} (Y^{oh}) and Ag^{oh}, which are, in contrast to the LT phase, ordered, leading to a layered structure. These structures can be classified as O1, as the unit cells contain only a single AgTe$_2$ layer.[58] Due to the increase in ordering, the unit cell volumes of the HT phases are smaller than the LT phases. However, whereas Tm atoms are fixed between Ag atoms in the c-direction, Ag and Te form honeycomb-like channels in the HT

phase of YAgTe$_2$ which are occupied by Y atoms in the center. The slight change in crystal structure is possibly a result of the larger ionic radius of Y^{3+} (0.90 Å) in contrast to Tm^{3+} (0.88 Å).[59]

Although the tetragonal phase of TmAgTe$_2$ is considered as the LT phase as it has a lower symmetry and the energy of the tetragonal phase was ~15 meV per atom lower than the trigonal phase in the computational study, Gulay *et al.* could obtain the trigonal phase at room temperature if the samples were annealed to 870 K and quenched in air.[60] We annealed the samples at 870 K, following by quenching the sample in water, confirming the trigonal phase. However, the trigonal phase slowly transformed at elevated temperature (650 K < T < 740 K) indicating that the trigonal phase is metastable at room temperature, as also discussed by Zhu *et al.*[22] The Mg- and Zn-doped TmAgTe$_2$ compounds crystallize in the HT trigonal phase, even if annealed at the same temperature as the parent compound, and no evidence of the LT tetragonal phase was observed. Thus, Mg- and Zn-doping on the Ag site seems to stabilize the material in the HT phase. The intrinsically doped YAgTe$_2$ compound, on the other hand, crystallizes in the same LT phase as the parent compound.

In contrast to the Ag-based compounds, both phases of YCuTe$_2$, the LT and HT phase, crystallized in the trigonal symmetry with space group $P\bar{3}m1$ (Fig. 1(e)) and $P\bar{3}$ (Fig. 1(f)), respectively. In both phases, Y atoms occupied the octahedral interstices, YCu$_6$ (Y^{oh}), and Cu atoms occupied tetrahedral interstices, CuTe$_4$ (Cuth), creating a layered structure. However, whereas the Cu atoms are completely disordered (*i.e.*, equivalent sites are randomly occupied) in the HT phase, the Cu atoms are partially disordered in the LT phase leading to two types of CuTe$_4$ tetrahedra. As shown in Fig. 1(e), the two types of tetrahedra result in a unit cell with two layers (A–B–A stacking): one layer consists solely of tetrahedra with disordered Cu atoms on the 6i site, and the other layer consists of a mixture of tetrahedra with disordered Cu atoms on the 6i site and ordered Cu atoms on 2d site (as discussed by Aydemir *et al.*).[23] Because Y occupied octahedral interstices in both phases, the LT and HT crystal structures can be described as O2 and O1, respectively.[58] Aydemir *et al.* also computed the energy difference between the LT and HT phases using the Ewald sum of six different configurations and found a consistent value of ~0.7 meV per atom, which is within the numerical tolerance of the calculation.[23] Furthermore, it is important to note that $P\bar{3}m1$ (Fig. 1(e)) is a subgroup of $P\bar{3}$ and the unit cell of the LT phase can be represented with a 2 × 2 × 2 supercell of the HT phase.

All LT phases and the HT phases of TmAgTe$_2$ and YCuTe$_2$ were confirmed using powder X-ray diffraction (PXRD) (see Fig. S2 in ESI†) and refined with the LeBail method. The refined parameters of the tetragonal and trigonal phase in TmAgTe$_2$ indicate that the unit cell volume of the trigonal phase ($a = b = 4.286$ Å and $c = 7.016$ Å, $V_{UC} = 112$ Å^3) is less than half of the tetragonal phase ($a = b = 7.091$ Å and $c = 4.526$ Å, $V_{UC} = 228$ Å^3). However, the number of unit formulae in the tetragonal phase is double the trigonal phase, resulting in similar theoretical densities. The HT trigonal phase parameters are also in agreement with the parameters reported by Gulay *et al.* ($a = b = 4.292$ Å and $c = 7.003$ Å).[60] The lattice parameters of the LT tetragonal

phase of YAgTe$_2$ compounds ($a = b = 7.149$ Å and $c = 4.593$ Å) agree well with those reported by Pardo *et al.* ($a = b = 7.126$ Å and $c = 4.581$ Å)[61] and Gulay *et al.* ($a = b = 7.140$ Å and $c = 4.595$ Å).[62] While Pardo *et al.* also acquired the PXRD pattern of the HT phase ($P\bar{3}$),[61] it was not feasible to record the pattern here due to the temperature limitation of the diffractometer. Y$_{0.98}$Ag$_{1.02}$Te$_{1.98}$ crystallizes in the same LT crystal structure as the parent compound but with slightly increased parameters. Since the LT phase of YCuTe$_2$ is a $2 \times 2 \times 2$ supercell, each lattice constant ($a = b = 8.606$ Å and $c = 13.837$ Å) is nearly twice that in the HT phases of TmAgTe$_2$ and YAgTe$_2$. Furthermore, supercell reflection peaks (*i.e.*, peaks of the $P\bar{3}m1$ structure) were observed for the parent YCuTe$_2$ compound at room temperature. However, the supercell peaks vanished with increasing temperature and Cu content, as reported by Aydemir *et al.*,[23] and no supercell reflection peak was recorded for Y$_{0.96}$Cu$_{1.08}$Te$_2$. As for doped TmAgTe$_2$ and YAgTe$_2$ compounds, Y$_{0.96}$Cu$_{1.08}$Te$_2$ has larger lattice parameters than the parent compound.

The lattice parameters also were calculated using first-principles calculations with and without the inclusion of dispersion-correction and compared to experiments (see Table 1). The calculated lattice parameters of the LT phases of TmAgTe$_2$ and YAgTe$_2$ indicate good agreement in the *a*- and *b*-direction (*i.e.*, parallel to the atomic layers) but a large overestimation of the lattice parameter in the *c*-direction (*i.e.*, perpendicular to the atomic layers) if dispersion-correction is not included in the first-principles calculations. The overestimation of the lattice constant most likely corresponds to an underestimation of the binding forces, a known shortfall of the PBE-GGA functional especially in layered structures.[63,64] London dispersion forces dominant in interlayer regions cannot be calculated by PBE-GGA and thus, a dispersion correction term has to be included, *e.g.*, using the exchange-hole dipole moment (XDM)[65,66] or DFT-D3 methods.[46] The dispersion is especially important for the calculation of thermal properties; an underestimation of the binding forces would lead to an underestimation of the lattice thermal conductivity and hence, an

overestimation of the thermoelectric performance. Therefore, the values were also computed with the inclusion of dispersion correction, leading to good agreement with experiments. The lattice parameters of the HT phase of TmAgTe$_2$ has good agreement, even without the inclusion of dispersion-correction (Table 1). The dispersion-correction is negligible in the HT phase as the distance between the layers is nearly twice that in the LT phase and the dispersion correction is proportional to r^{-6} where r is the distance between atoms.[64] Furthermore, the ionic forces between the negative charged layers and the positive ions are significantly larger than the dispersion forces. Thus, the thermoelectric properties of LT-TmAgTe$_2$ and LT-YAgTe$_2$ were only investigated using the optimized crystal structure with DFT-D3.

To analyse the thermoelectric performance, it is necessary to understand the temperature ranges of the individual phases because the thermoelectric transport properties are strongly related to the crystal structures. Thus, DSC thermograms of TmAgTe$_2$ and YAgTe$_2$ were recorded (Fig. S3;† thermogram of YCuTe$_2$ can be found in ref. 23). Prior the experiments it was confirmed that all compounds were in the LT phase (*i.e.*, TmAgTe$_2$ is in the tetragonal phase). All XYZ_2 compounds show reversible phase transitions, including the LT-TmAgTe$_2$ phase. While Zhu *et al.* reported only a first-order phase transition in TmAgTe$_2$ from the tetragonal to the trigonal phase between 725–735 K,[22] in the present study an additional subtle phase transition was observed at 650 K. (Onset temperatures, change of enthalpy, and change of entropy of XYZ_2 compounds are presented in Table S2†). Furthermore, supercooling was observed in TmAgTe$_2$ but not in the other two compounds. Supercooling indicates that the dynamics through the solid–solid phase transition are slow and it takes a long time to re-form the LT phase on cooling. This result is consistent with the PXRD pattern recorded after the DSC measurement which showed that the HT-TmAgTe$_2$ phase was not completely transformed back to the LT phase.

YAgTe$_2$, like TmAgTe$_2$, has two first-order phase transitions (Fig. S3(b)†). However, these phase transitions are weaker than

Table 1 Computational and experimental lattice parameters of TmAgTe$_2$, YAgTe$_2$, and YCuTe$_2$. Computational parameters were calculated with PBE-GGA with and without inclusion of dispersion correction (DFT-D3). Experimental results were determined using the Le Bail refinement method

Compound	Space group	PBE-GGA/Å	PBE-GGA with DFT-D3/Å	Exp./Å
TmAgTe$_2$	$P\bar{4}2_1m$	$a = b = 7.072$, $c = 4.684$	$a = b = 7.061$, $c = 4.532$	$a = b = 7.091$, $c = 4.526$ $a = b = 7.0831$, $c = 4.5298$ (ref. 22)
TmAgTe$_2$	$P\bar{3}m1$	$a = b = 4.342$, $c = 6.998$		$a = b = 4.298$, $c = 7.037$ $a = b = 4.295$, $c = 7.007$ (ref. 22) $a = b = 4.292$, $c = 7.003$ (ref. 60)
TmMg$_{0.05}$Ag$_{0.95}$Te$_2$	$P\bar{3}m1$			$a = b = 4.305$, $c = 7.016$
TmZn$_{0.05}$Ag$_{0.95}$Te$_2$	$P\bar{3}m1$			$a = b = 4.298$, $c = 7.021$
YAgTe$_2$	$P\bar{4}2_1m$	$a = b = 7.126$, $c = 4.742$	$a = b = 7.120$, $c = 4.580$	$a = b = 7.149$, $c = 4.593$ $a = b = 7.126$, $c = 4.581$ (ref. 61) $a = b = 7.140$, $c = 4.595$ (ref. 62)
Y$_{0.98}$Ag$_{1.02}$Te$_{1.98}$	$P\bar{4}2_1m$			$a = b = 7.154$, $c = 4.604$
YCuTe$_2$	$P\bar{3}m1$			$a = b = 8.634$, $c = 13.837$ $a = b = 8.614$, $c = 13.829$ (ref. 23)
Y$_{0.96}$Ag$_{1.08}$Te$_2$	$P\bar{3}m1$			$a = b = 8.649$, $c = 13.841$

those of $TmAgTe_2$ and no supercooling was observed in $YAgTe_2$, indicating faster transition dynamics. That is reasonable because the Ag atoms fill the tetrahedral interstices in both the LT and HT phase of $YAgTe_2$ whereas the Ag atoms switch from the tetrahedral interstices in the LT phase of $TmAgTe_2$ to an octahedral environment in the HT phase. In contrast to the two phase transitions reported here, Pardo *et al.* recorded only a single phase transition at 793 K, higher than the present onset temperature (see Table S1†).[61] The difference between the thermal profiles shown by Pardo *et al.* and the present study might be due to slightly different compositions. A single first-order phase transition at lower temperatures was observed for $YCuTe_2$. The phase transition is rather subtle and can be attributed to a small change in crystal structure. The phase transition in $YCuTe_2$ is discussed further in ref. 23.

3.2. Electrical properties

The electronic band structure of LT-$TmAgTe_2$ computed with PBE-GGA exhibits multiply nearly degenerate bands close to the valence band maximum (VBM) with strong curvature, suggesting enhanced electronic properties (*i.e.*, power factor, PF = σS^2) (Fig. 2). The valence band has a maximum at the Γ point, where three bands are almost degenerate in the NSOC band structure. Additionally, two valence bands at the A point could contribute to PF at elevated temperature, suggesting enhanced p-type PFs in LT-$TmAgTe_2$. However, with the inclusion of spin–orbit coupling (SOC), the degeneracy at the VBM breaks, resulting in a reduction in PF. While the split of the degenerate bands has been observed for several compounds containing heavy elements,[67,68] the breaking of the degeneracy at the VBM using an optimized crystal structure with inclusion of van der Waals
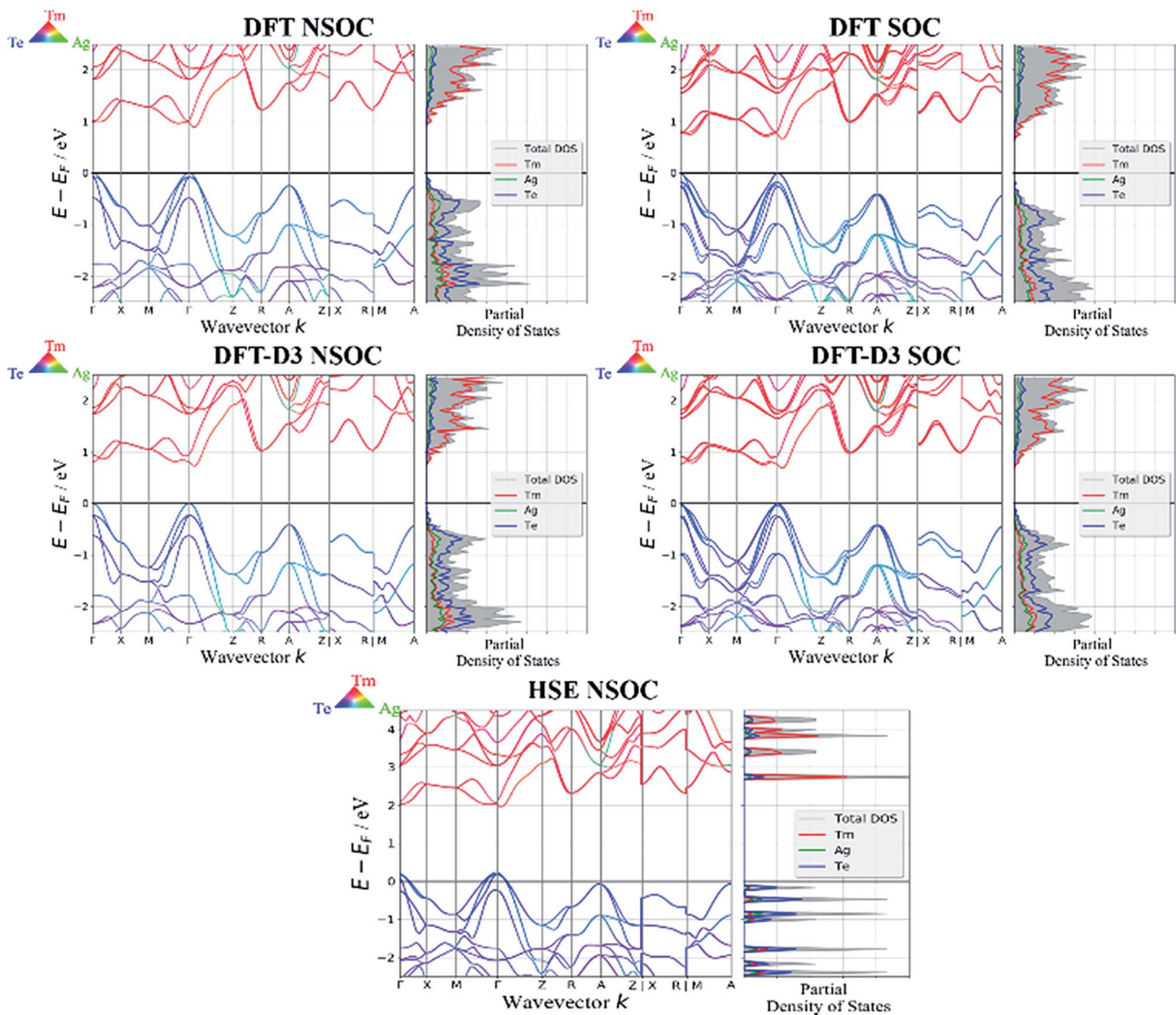

Fig. 2 Electronic band structures of LT-$TmAgTe_2$ using PBE-GGA with and without the inclusion of spin−orbit coupling (SOC) and van der Waals interactions (DFT-D3) as well as using HSE06 without including spin−orbit coupling (NSOC). The degeneracy of the valence bands at the Γ points breaks due to SOC and/or DFT-D3. The different colors in the electronic band structure represent the contributions of different elements to the various band structures.

interactions has not been reported previously. The degeneracy of the valence bands is sensitive to the local symmetry of the bonds which can be greatly influenced by van der Waals interactions. Fig. 2 shows that the VBM is dominated by p-orbitals of Te. Each of the two equivalent Te atoms in the unit cell forms two equivalent bonds with Ag atoms and three different bonds with Tm atoms. The three bands at the VBM can be separated into one Te–Ag band (i.e., hybridization of Te [p-orbitals] and Ag [d- and p-orbitals]) and two degenerate Te–Tm–Ag bands (i.e., Tm [p- and d-orbitals] hybridizes with Te and Ag) ensured by symmetry. Given the varied wave function character difference between Te–Ag band and two degenerate Te–Ag–Tm bands at the VBM, a change in bond length could lead to an energy difference between the Te–Ag and Te–Tm–Ag bands.[69] In the DFT-relaxed structure, the energy difference between the Te–Ag band and Te–Tm–Ag bands is small and the three bands are nearly degenerate. However, with the inclusion of DFT-D3, the bond distance of Te–Ag decreases from 2.890 Å to 2.872 Å (<1%) and the three bond distances of Tm–Te are reduced from 3.035 Å to 3.023 Å (<1%), 3.011 Å to 3.000 Å (<1%) and 3.144 Å to 3.075 Å (>2%), respectively. The large difference between DFT and DFT-D3 optimized Te–Tm bonds compared to Te–Ag could lead to a larger split of the nearly degenerate bands at the VBM.

Further explanation can be provided by the bonding and anti-bonding states of the Te–Tm–Ag bands and Te–Ag bands (Fig. S4†). While the Te–Ag bands at the VBM have anti-bonding character, the Te–Tm–Ag bands have a combination of anti-bonding character in the Te–Ag band and ionic character between Tm and the Te–Ag band. With an increase in inter-atomic forces, the ionic bonding states of the Te–Tm–Ag bands are more repulsive leading to a larger split of the valence and conduction states. However, the anti-bonding orbitals of the Te–Ag bands are pushed upwards with the inclusion of dispersion forces reducing the degeneracy of the bands and also decreasing the band gap energy by 0.26 eV as observed in Fig. 2. (Further discussion of the bonding states can be found in the ESI.) A similar reduction in band gap energy was reported for various transition-metal dichalcogenides.[30] This can also be depicted by the Fermi surfaces of LT-TmAgTe$_2$ which indicate a split of Te–Tm–Ag bands with the inclusion of SOC (Fig. S5†).

In contrast to the optimized crystal structure, spin orbit coupling effects will split the two degenerate Te–Tm–Ag bands giving the result that the VBM is one of the split Te–Tm–Ag bands. In the DFT relaxed structure, the energy differences in Te–Ag band and Te–Tm–Ag degenerate bands are small without SOC ($\sim$0.07 eV), leading to a large difference between Te–Tm–Ag band at VBM and Te–Ag band with inclusion of SOC (Fig. 2). Interestingly, since the Te–Tm–Ag bands lie $\sim$0.24 eV below the Te–Ag band in the dispersion-optimized electronic band structure, inclusion of SOC pushes one Te–Tm–Ag band to the Te–Ag band. As a consequence, the Te–Ag band overlaps with the upper Te–Tm–Ag band resulting in a degeneracy of two for the DFT-D3 SOC band structure. Therefore, a higher Seebeck coefficient is expected compared to that from the DFT-D3 NSOC band structure. The same behavior is observed in LT-YAgTe$_2$ (Fig. S6†), which is not surprising as Te and Ag contribute mostly to the VBM in LT-TmAgTe$_2$ and LT-YAgTe$_2$. The

difference in the shapes of the bands between GGA NSOC and HSE NOC of LT-TmAgTe$_2$ is insignificant (Fig. 2) and hence, the electronic properties can be calculated with the band structure of PBE-GGA where the band gap is corrected to that of HSE06.

In addition to the LT tetragonal phases of TmAgTe$_2$ and YAgTe$_2$, the electronic band structure of HT-TmAgTe$_2$ was computed. The valence bands have multiple bands at the high symmetry point A and along the Σ and Λ lines with multiplicities of 1, 6, and 6, respectively (Fig. S7†). The HT-phase shows a reduction of the band gap to $\sim$0.39 eV ($\sim$0.69 eV) with (without) inclusion of SOC. Higher band gap energies were obtained when the screened hybrid functional HSE06 was applied and SOC is not included (NSOC) (Table S4†). The inclusion of SOC would be too computationally expensive to use the HSE06 functional and would exceed the scope of this study. However, HSE06 applied to the DFT-D3 relaxed structure leads to band gaps energies of 1.36 eV for both LT phases of TmAgTe$_2$ and YAgTe$_2$ (Table S4†). The HSE06 functional overestimates the experimental band gap ($E_g = 0.54$ eV)[22] almost by a factor of three and the experimental band gap energy can be reasonably approximated by the GGA-band gap. Note that SOC can further reduce the band gap energy and enhance the prediction of the electronic properties.

The LT and HT phases of YCuTe$_2$ have different band structures although the LT phase is a sub-space group of the HT phase (Fig. S8 and S9†). Both band structures have multiple degenerate bands at the VBM. But the valence bands of the HT phase exhibit a lower effective mass at the VBM than the LT phase, consisting with reducing the electrical resistivity and the Seebeck coefficient. The low effective mass in the HT phase also leads to a larger band separation between the light and heavy hole band at the Γ symmetry point with SOC ($\sim$0.7 eV). The conduction bands of HT-YCuTe$_2$ have minima at M and L, which contribute to the n-type electronic properties, and they are separated by an energy of 0.13 eV (NSOC). The energy difference slightly decreased to 0.11 eV with the inclusion of SOC and the electronic band structures of YCuTe$_2$ suggest that YCuTe$_2$ has good p- and n-type electronic behavior. Note that the experimental band gap of LT-YCuTe$_2$ ($E_g = 0.60$ eV)[23] is slightly higher than the GGA-NSOC band gap and almost half the band gap energy of the HSE06.

As the Seebeck coefficient is strongly dependent on the electronic DOS, the experimental DOS of several XYZ_2 compounds (LT-TmAgTe$_2$, HT-TmAgTe$_2$, TmMg$_{0.05}$Ag$_{0.95}$Te$_2$, YAgTe$_2$, YCuTe$_2$, and Y$_{0.96}$Cu$_{1.08}$Te$_2$) were determined at the Fermi level using UPS and IPES (Fig. 3). The experimental DOS of the LT- and HT-phases of TmAgTe$_2$ are similar, showing three peaks at -2.5 eV, -6 eV, and -10.3 eV (Fig. 3(a) and (b)). While the peaks at -6 eV and -10.3 eV can be assigned to Ag-d and Te-s, respectively, Te-p contributes mainly to the peak that is close to the Fermi level. The LT-phase contains an additional peak at slightly higher binding energy ($E - E_F = -12.3$ eV) and the Ag-d peak is suppressed compared to Te-p peak, consisting with our calculations. Above the Fermi level, the DOS of both LT- and HT-TmAgTe$_2$ is nearly the same. However, the Mg-doped sample exhibits a distinct peak above the Fermi energy while this feature is missing in the valence band. Furthermore,
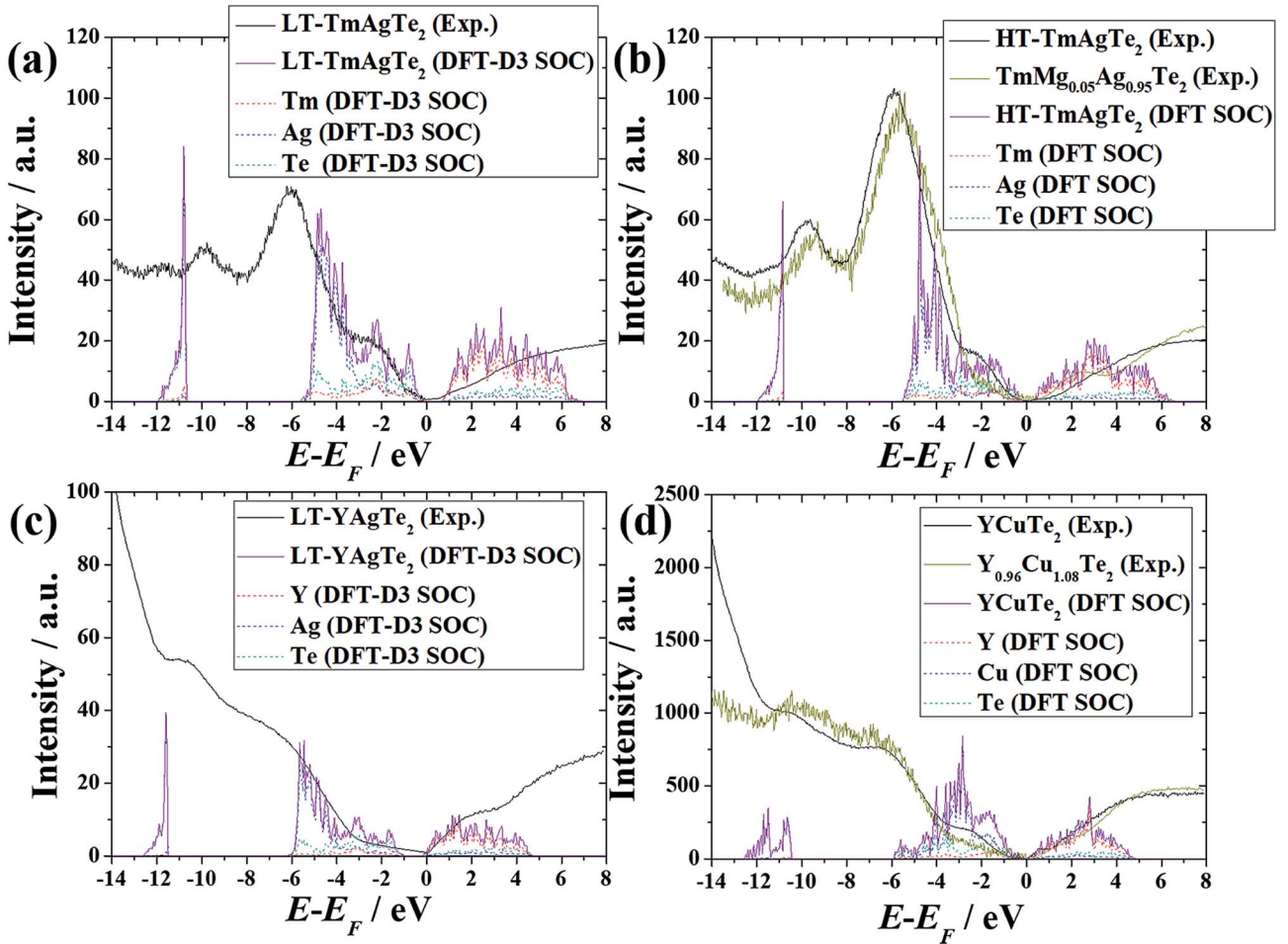
Fig. 3 Computed DOS, partial density of states (pDOS), and experimental DOS using UPS/IPES for (a) LT-TmAgTe$_2$, (b) HT-TmAgTe$_2$, (c) YAgTe$_2$, and (d) YCuTe$_2$. Although UPS spectra using a He II source indicate more features at the valence band maximum, the signal-to-noise ratio was, in YAgTe$_2$ and YCuTe$_2$, too large and therefore, a He I source was used for their measurement. The pDOS was computed using PBE-GGA and SOC. Note that for LT-TmAgTe$_2$ and YAgTe$_2$, the DFT-D3 optimized band structure was used for the computation of pDOS.

the computed DOS of Te-s and Ag-d were shifted to lower binding energies compared to experiments. It is important to note that no f-electrons were considered as valence electrons and the inclusion of f valence electrons for Tm can influence the positions of the Te-p and Ag-d DOS.

The experimental DOS of YAgTe$_2$ indicates a peak at −10.8 eV, which has a slightly higher binding energy than TmAgTe$_2$ (Fig. 3(c)). A higher binding energy was also calculated for the Te-p peak compared to the peak in LT-TmAgTe$_2$, in agreement with experiments. Furthermore, a shoulder was recorded at −7 eV, which can be assigned to the Ag-d peak. In both YCuTe$_2$ samples, two peaks were observed ($E − E_F = −6.8$ eV and $−10.6$ eV) and the peak at −10.6 eV can be assigned to Te-p (Fig. 3(d)). This is in agreement with the computed peak for Te-p ($E − E_F = −10.7$ eV) using PBE-GGA and SOC. The intrinsic YCuTe$_2$ has a similar experimental DOS. However, the DOS of Y$_{0.96}$Cu$_{1.08}$Te$_2$ is lower at the VBM than the parent compound, which might point to an increase in electrical conductivity and a decrease in Seebeck coefficient.

As the computed DOS agrees well with experiments, the electronic properties were calculated using Boltzmann transport equations. In a previous study, Chen et al. reported that the computed electrical conductivity is, in general, dramatically overestimated whereas the experimental Seebeck coefficient has a strong correlation with the computed values.[25] For Chen's study, a universal constant relaxation time (UCRL) of $\tau = 10^{-14}$ s was applied for the calculation of the electrical conductivity. (The electronic properties of more than 48 000 inorganic compounds used in Chen's study were recently published by Ricci et al.).[70] Note that the relaxation time depends on several factors, such as microstructure, carrier concentration, temperature and energy. More accurate estimation of the relaxation time likely would improve the prediction of the computed electrical conductivity.

It was found in several thermoelectric materials that the relaxation time is limited by acoustic phonon scattering at high temperature.[71–73] Therefore, the electrical resistivity was calculated in the present study with a temperature-dependent relaxation time limited by acoustic phonon scattering $\left(\tau = \tau_0\left(\dfrac{T}{300\ \text{K}}\right)^{-1}\right)$ where $\tau_0 = 1.5 \times 10^{-15}$ s for the TmAgTe$_2$

and $\tau_0 = 1.0 \times 10^{-14}$ s for the other compounds investigated. For the calculation of the electrical properties, the carrier concentration and temperature were set to experimental values. The temperature-dependent electrical resistivity reveals good agreement between experiments and computations over temperature (Fig. 4). In particular, the computed electrical resistivity of LT-TmAgTe$_2$ has a similar temperature trend to the experimental data. Furthermore, the electrical resistivity calculated from electronic band structures using the PBE exchange–correlation functional is nearly the same as that from the HSE06 exchange–correlation functional. However, if SOC was included in the calculation, the electrical resistivity decreased, and the computed data revealed a stronger correlation with experiments. It is important to note that the computed electronic properties labelled as HSE-NSOC were calculated from the PBE-GGA band structure corrected to the band gap of the HSE06 exchange–correlation functional because the band structures using PBE-GGA and HSE06 have similar band shapes. All investigated XYZ_2 compounds have a band gap > 0.25 eV, where at low temperature the intrinsic effects (bipolar) can be neglected and the extrinsic effects (*i.e.*, band shape) predominantly contribute to the electronic properties. At high temperature the contribution of the intrinsic (bipolar) effects to the electrical resistivity increases and hence, a slight decrease in resistivity was observed with temperature for the PBE band structures of HT-TmAgTe$_2$ and LT-YCuTe$_2$.

Fig. 4(b) indicates that the calculated electrical resistivity of HT-TmAgTe$_2$ with the inclusion of SOC exhibits good agreement with experiment to ~650 K. At higher temperatures, the electrical resistivity decreases, most likely due to intrinsic (bipolar) effects. A larger band gap would reduce the bipolar effect and hence increase the electrical resistivity, as shown for the resistivities from the NSOC band structures. An increase in electrical resistivity was found above 500 K, which can be

attributed to the band shape using NSOC. However, while the HSE resistivity increased rapidly at high temperature, the PBE-calculated resistivity approaches a plateau due to intrinsic effects. The PBE-SOC band gap is lower than that for the PBE-NSOC resulting in a higher contribution of intrinsic effects and hence, reduction in electrical resistivity. These comparisons indicate that the intrinsic (bipolar) contribution can be significant at high temperature (where the thermal energy is less than 20% of the band gap energy).[74] Therefore, the enhancement of electronic properties using the HSE06 exchange correlation functional is insignificant at low temperatures (T < 700 K) if the PBE-GGA band gap energy is moderate (PBE-GGA band gap > 0.5 eV). The large discrepancy between the computed and experimental electrical resistivities in YAgTe$_2$ (Fig. 4(c)) is most likely a result of the large uncertainty in the Hall coefficient as the computed resistivity was calculated from the experimental Hall carrier concentration.

To quantify the prediction of the electrical resistivity using different band structures, the average relative deviations were calculated over temperature, which indicates that SOC dramatically enhanced the prediction of the electron transport in XYZ_2 compounds while HSE reveals even weaker correlation than the corresponding PBE-GGA-calculated resistivities (Table S4†). The larger deviations of the HSE structure can be attributed to the large overestimation of the band gap energy in the XYZ_2 compounds. Whereas SOC plays a significant role in the prediction of the electrical resistivity for the band structures without DFT-D3, the resistivity of the band structures with the inclusion of van der Waals interactions reveals good agreement with experiments, even for the NSOC band structures. The differences for the three methods (PBE with and without SOC, and HSE without SOC) for the structure-optimized electronic band structures is small. Furthermore, the maximum relative deviations of the band structure with DFT-D3 are smaller than that for the corresponding DFT values without the inclusion of SOC. Therefore, the uncertainty of the electrical resistivity at various temperatures is less significantly over- or under-estimated using DFT-D3. Note that with the exception of TmAgTe$_2$ (because it would underestimate the electrical resistivity by nearly one order of magnitude) τ_0 was not adjusted and the prediction of the electrical resistivity likely can be enhanced by a better estimation of τ_0.

In addition to the electrical resistivity, the experimental Seebeck coefficient was compared to the computational values (Fig. 5). All investigated and reported XYZ_2 compounds[22–24] show positive Seebeck coefficients, suggesting that holes are the dominant charge carriers over the entire temperature range.

The computed Seebeck coefficients of TmAgTe$_2$ using NSOC-band structures agree well with the experimental data (Fig. 5(a) and (b)) whereas the Seebeck coefficient decreased when SOC was applied, due to a splitting of the degenerate valence bands. While this trend is well known, the opposite behavior was observed for the DFT-D3 structure where the SOC band structure exhibits a higher Seebeck coefficient than the corresponding NSOC band structures; a similar trend was observed for LT-YAgTe$_2$ (Fig. 5(c)). This is surprising as SOC generally splits the degenerate bands and a reduction in the Seebeck
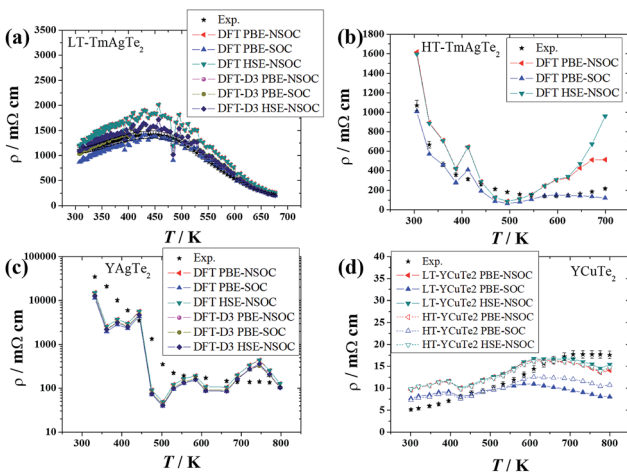

Fig. 4 Computed and experimental electrical resistivity of (a) LT-TmAgTe$_2$, (b) HT-TmAgTe$_2$, (c) YAgTe$_2$, and (d) YCuTe$_2$. The computed electrical resistivity agrees well with experiments. The carrier concentration and temperature for the calculations were taken from experiments. Experimental resistivities for LT- and HT-TmAgTe$_2$ were taken from Zhu *et al.*[22] and for YCuTe$_2$ were taken from Aydemir *et al.*[23]
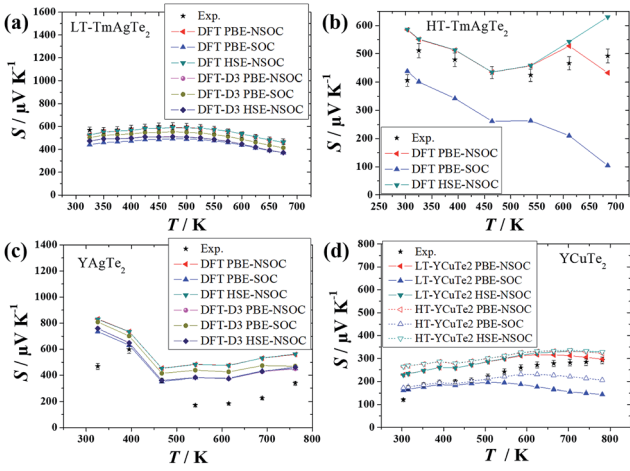
Fig. 5 Computed and experimental Seebeck coefficient of (a) LT-$TmAgTe_2$, (b) HT-$TmAgTe_2$, (c) $YAgTe_2$, and (d) $YCuTe_2$. The carrier concentration and temperature for the calculations were taken from experiments. Experimental Seebeck coefficient for LT- and HT-$TmAgTe_2$ were taken from Zhu et al.[22] and for $YCuTe_2$ was taken from Aydemir et al.[23]

Fig. 6 Experimental electrical resistivity of (a) $TmAgTe_2$ and (b) $YAgTe_2$ compounds indicating semiconducting behavior. The experimental Seebeck coefficient of (c) $TmAgTe_2$ and (d) $YAgTe_2$ is high due to a low carrier concentration. For comparison with the parent compound high-temperature electrical properties of LT-$TmAgTe_2$ (tetr.) and HT-$TmAgTe_2$ (tri.) were taken from Zhu et al.[22]

coefficient would be expected. The temperature-dependent Seebeck coefficient calculated from the crystal structures without van der Waals has a smaller absolute relative deviation for LT-$TmAgTe_2$ and a larger one for the LT-$YAgTe_2$, relative to the DFT-D3 Seebeck coefficients (Table S5†). Note especially that the Seebeck coefficients of LT-$TmAgTe_2$ computed from the PBE-GGA band structure without SOC and van der Waals interactions have strong correlation with the experimental data (average relative deviation <2%). The average relative deviation of the Seebeck coefficient (Table S5†) is generally lower than the electrical resistivity (Table S4†), as also found by Chen et al.[25] However, the difference between the resistivity and Seebeck coefficient is less significant than in the previous report by Chen et al.[25] The better agreement with the resistivity here can be attributed to the implementation of a temperature-dependent relaxation time which does not lead to a large overestimation of the resistivity at high temperature.

In addition to the previously investigated $TmAgTe_2$ (ref. 22) and $YCuTe_2$ (ref. 23) compounds, the temperature-dependent electrical properties of extrinsically doped $TmAgTe_2$ and $YAgTe_2$ compounds were measured in the present study (Fig. 6). The electrical resistivity of the $TmAgTe_2$ compounds in the trigonal phase show a temperature trend similar to the extrinsically doped compounds and decreased with temperature pointing to intrinsic semiconducting behavior. The carrier concentration of the doped-$TmAgTe_2$ compounds increased compared to the parent compound and hence the resistivity decreased compared to the HT phase of $TmAgTe_2$ (Fig. 6(a)). In particular, the Zn-doped compound has nearly one order of magnitude higher hole carrier concentration than HT-$TmAgTe_2$ (Fig. S10(b)†). Although the higher hole concentration (above 550 K) resulted in a reduction of the electrical resistivity, the Seebeck coefficient was not reduced, and thus a higher power factor was achieved for the Zn-doped samples. The increase in
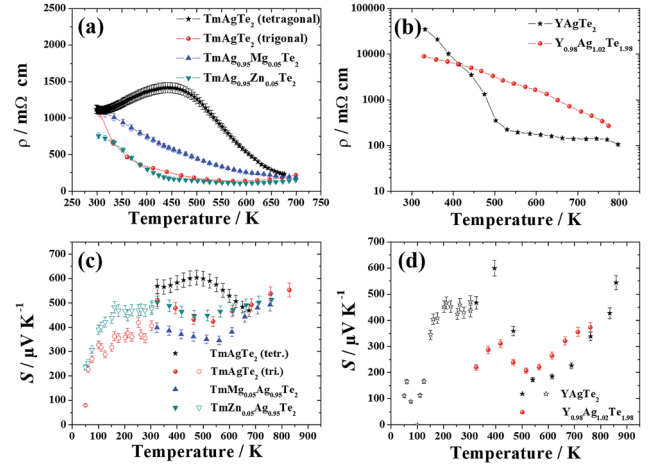
hole carrier concentrations is surprising as the divalent Zn atom on the monovalent Ag side should decrease the hole carrier concentration. The increase in hole carrier concentration can be explained using the ionic radii. Ag^+ has the largest ionic radius (100 pm), followed by Tm^{3+} (88 pm) and Zn^{2+}/Mg^{2+} (60/57 pm).[59] Previous defect calculations indicated that the hole carrier concentration in HT-$TmAgTe_2$ is limited by Tm_{Ag}-antisite defects acting as hole killers.[22] It is likely that Tm_{Ag}-antisite defects occur also in the Zn-doped $TmAgTe_2$ compound. However, Zn^{2+} could occupy the empty Tm^{3+} site, which would generate a hole and hence, would increase the hole carrier concentration. This is also consistent with the slight decrease in the lattice parameters of the Zn-doped sample. Further defect calculations are required to understand the increase in carrier concentration.

Poorer electrical properties were observed for $YAgTe_2$ most likely due to a low mobility (Fig. 5(c) and S11(a)). While the carrier concentration is higher than the Zn-doped $TmAgTe_2$ compound, the electrical resistivity is more than one order of magnitude higher than the $TmAgTe_2$ compounds at room temperature. Despite the high resistivity, the magnitude of the Seebeck coefficient of $YAgTe_2$ is low and thus the electrical properties of $YAgTe_2$ are not useful for high-performance thermoelectric materials. No apparent mechanical degradation (e.g., cracking) was observed after the transport measurements. To confirm the mechanical stability and repeatability of the measurements, ρ of $YCuTe_2$ was measured on heating and cooling and no significant change in ρ was observed (Fig. S12†).

3.3. Thermal properties

In addition to the electronic properties, the thermal properties of XYZ_2 compounds were also investigated, to better understand the accuracy of the computation as well as the potential of those materials as thermoelectrics. For the previous high-throughput

screening, Zhu *et al.* used a fixed phononic contribution to the thermal conductivity ($\kappa_p = 0.5$ W m^{-1} K^{-1}) to determine the theoretical zT.[22] However, κ_p depends on several factors, *e.g.*, crystallinity, microstructure, crystal structure, and temperature, and it is currently not feasible to calculate κ_p in a high-throughput approach (except for simple crystal structures).[75] Insight concerning κ_p can be provided by the lowest limit of thermal conductivity (κ_{min}). The most common approach to calculate κ_{min} was established by Cahill *et al.*[38,39] However, several materials show experimental thermal conductivities lower than their theoretical κ_{min}, and are referred to as having ultralow thermal conductivity. Recently, Pöhls *et al.* developed a new model for κ_{min}, in which the thermal energy is transported between entities of phonons and limited by the phonon mean speed, and used it to delineate the origins of ultralow thermal conductivity in PCBM.[20,40] The phonon mean free path can be frequency-independent (for static disordering) or frequency-dependent (for dynamic disordering, *i.e.*, two-phonon processes) and the phonon mean speed can be determined from phonon dispersion curves.[20]

For the phonon dispersion curves calculations of LT-TmAgTe$_2$ and LT-YAgTe$_2$, van der Waals interactions were included to enhance the accuracy of the forces calculations between the layers. Note the phonon dispersion curve for YCuTe$_2$ was calculated from the monoclinic space group $C2/m$ instead of $P\bar{3}m1$, as observed from experiments because the disordering of the Cu atoms can be better simulated in less symmetric space groups and the monoclinic space group $C2/m$ had the lowest energy of all low-symmetric space groups (monoclinic/triclinic). The disordered structure was approximated by setting the Cu occupations of the 6i site that is far from the 2d site to be 2/3 and the 6i site that is near the 2d site to be 1/3.

The investigated phonon dispersion curves point to a low lattice thermal conductivity. For instance, the maximum frequency of the optical modes for the three investigated compounds was low (180 cm^{-1}) and most of the optical modes are nearly dispersionless, leading to a low phonon group velocity. Thus, the contribution of the optical modes to the thermal conductivity can be considered as insignificant (Fig. 7). Furthermore, all dispersion curves contain low-frequency optical modes (<50 cm^{-1}), which suppress the acoustic modes, leading to a low acoustic contribution to the thermal conductivity. The acoustic modes increase nearly linearly from the center of the Brillouin zone for all dispersion curves and thus, the phonon mean speed can be determined using the Debye model. The Debye temperatures, calculated from the phonon dispersion curves, were extremely low for all three compounds and hence a low thermal conductivity would be expected. The lowest Debye temperature was determined for YAgTe$_2$ ($\theta_D = 107$ K [with inclusion of DFT-D3]), followed by TmAgTe$_2$ and YCuTe$_2$ (Table S6†). To investigate the influence of crystal-structure optimization using van der Waals interactions, the phonon dispersion curves of YAgTe$_2$ were calculated with and without DFT-D3 (Fig. 7(b) and (c)). A small increase in frequency was observed when the van der Waals correction is included, due to an increase of the interatomic forces.
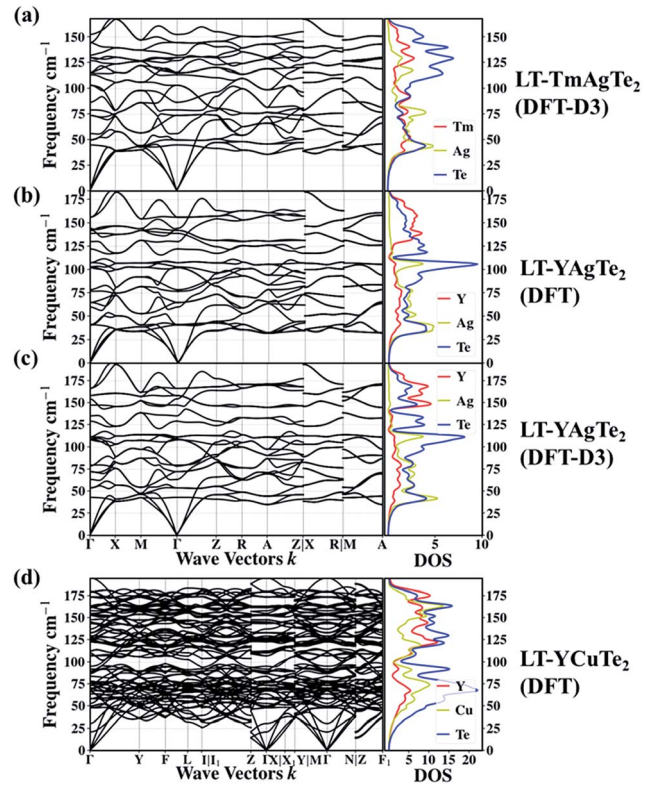

Fig. 7 Computed phonon dispersion curves of (a) LT-TmAgTe$_2$ (DFT-D3), (b) LT-YAgTe$_2$ (DFT), (c) LT-YAgTe$_2$ (DFT-D3), and (d) the monoclinic phase of YCuTe$_2$. The partial phonon DOS of the individual elements is provided to depict the contributions of the elements to the dispersions.

To check the calculated Debye temperature and the computed phonon dispersion curves, the heat capacities of the investigated compounds were measured and compared to the computed heat capacity from the phonon dispersion curves (Fig. 8). Whereas the computed heat capacity rapidly approached the Dulong–Petit value, the experimental heat capacity is higher at elevated temperature for all three compounds. The reason for the difference is most likely due to work from thermal expansion as the experimental heat capacity is at constant pressure, C_p, while the calculated value is at constant volume, C_V.

The smallest high-temperature difference between experimental and calculated heat capacity for a parent compound was observed for the TmAgTe$_2$: C_p is nearly constant above 200 K. Even smaller heat capacity differences were found for the extrinsically doped TmAgTe$_2$ compounds. The heat capacities of both extrinsically doped compounds are nearly the same over the entire temperature range suggesting that the difference between the heat capacity of the parent compound and the extrinsically doped compounds is related to the crystal structure. The extrinsically doped compounds crystallized in the HT (trigonal) phase while the parent compound was in the LT (tetragonal phase). The difference in $C_p - C_V$ can be estimated from
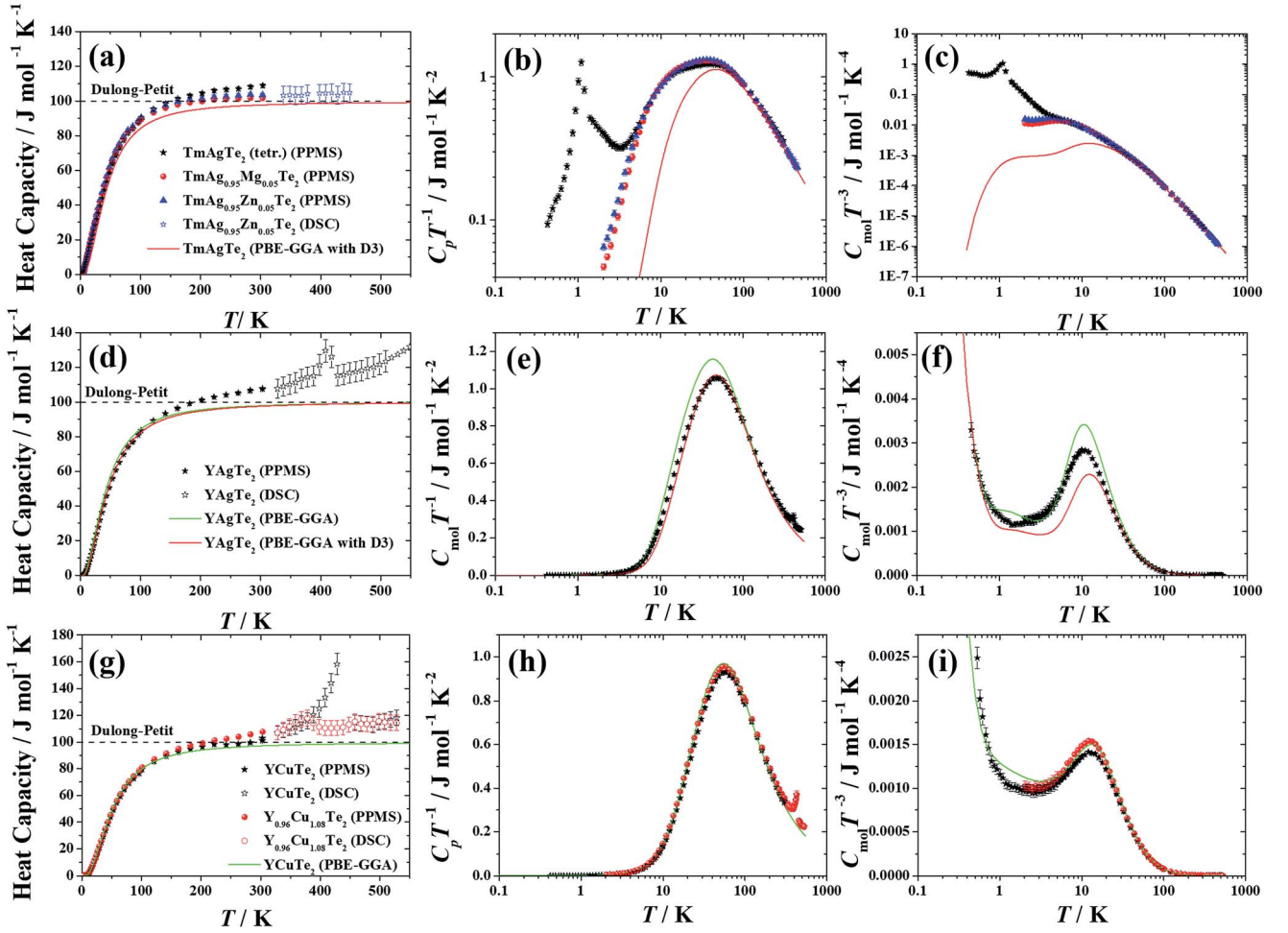
$$C_p - C_V = V_m T \frac{\alpha_V^2}{\beta_T} \tag{5}$$

Fig. 8 Comparison of computed and experimental heat capacity of (a–c) $TmAgTe_2$, (d–f) $YAgTe_2$, and (g–i) $YCuTe_2$. The heat capacity was divided by T (to emphasize the intermediate-temperature range) and T^3 (to emphasize the low-temperature range). An overestimation of the computed heat capacity was observed without van der Waals forces whereas an underestimation was observed when van der Waals forces were included. High-temperature heat capacity of $TmAgTe_2$ and $YCuTe_2/Y_{0.96}Cu_{1.08}Te_2$ were taken from Zhu *et al.*[22] and Aydemir *et al.*,[23] respectively.

where V_m is the molar volume, α_V is the coefficient of volumetric coefficient (under the assumption of isotropic behavior, $\alpha_V = 3\alpha$ where α is the linear coefficient of expansion), and β_T is the isothermal compressibility. Although thermal expansion is not isotropic for layered structures, the investigated pellets are polycrystalline and hence, most likely expand similarly in all directions. $C_p - C_V$ for $TmAgTe_2$ was calculated from the experimental unit cell volume and the coefficient of linear expansion ($\alpha = [20 \pm 2] \times 10^{-6}$ K^{-1} [Fig. S13; Table S7†]) as well as the calculated bulk modulus (reciprocal value of β_T) of 60.7 GPa, computed using the method by de Jong *et al.*[76] The resulting $C_p - C_V = 3.6$ J mol^{-1} K^{-1} is nearly a third of the difference between the experiments and computation for the LT-phase of $TmAgTe_2$ (10.7 J mol^{-1} K^{-1}). A similar $C_p - C_V$ was estimated for the other XYZ_2 compounds where a slightly higher coefficient of linear expansion was measured for $YCuTe_2$ ($\alpha = [27 \pm 2] \times 10^{-6}$ K^{-1} [Table S7†]).

This is consistent with a larger increase in heat capacity at elevated temperature observed for $YCuTe_2$. An even larger increase in heat capacity was observed for $YAgTe_2$. Both

compounds exhibit a phase transition, in agreement with the DSC thermograms. However, whereas the heat capacity is nearly constant for $YCuTe_2$ above the phase transition, the heat capacity further increased in $YAgTe_2$ suggesting that $YAgTe_2$ transforms from the LT-phase to a mixed phase; a second transition is observed in the DSC thermogram most likely to the HT phase as reported by Pardo *et al.*[61] The same behavior was observed in the coefficient of linear expansion where the average coefficient of linear expansion of $TmAgTe_2$ and $YCuTe_2$ is constant over a wide range of temperature and the coefficient for $YAgTe_2$ changes constantly (Fig. S13†). In addition to the experimental values, the theoretical coefficient of volumetric expansion was calculated from first principles (Table S7†). The theoretical coefficients of volumetric expansion are lower than the experimental values for LT-$TmAgTe_2$ but higher for $YAgTe_2$. Under consideration that computation can have a uncertainty of 15% (as reported for elastic properties),[76] the computed values are within the uncertainty of experiments.

To emphasize the intermediate-temperature and low-temperature ranges, C_p/T and C_p/T^3, respectively, were

considered (Fig. 8). The measured heat capacities of YAgTe$_2$ and YCuTe$_2$ agree well with the computed values. However, the computed heat capacity of TmAgTe$_2$ is underestimated at low temperature, which could be the result of several factors. For example, a low-temperature phase transformation was observed, which is most likely a second-order phase transformation as observed for TmB$_{50}$ (ref. 77) and Er$_2$Ti$_2$O$_7$.[78,79] No phase transition was observed for YAgTe$_2$, indicating that the phase transition is related to Tm. A similar low-temperature phase transition was observed in TmB$_{50}$ due to magnetic ordering.[77] Another reason could be the underestimation of the binding energy because most of the f electrons in Tm were treated as core electrons. An increase in binding energy would reduce the phonon frequencies and also the discrepancy between computed and experimental heat capacity. Broad peaks in C_p/T^3 were observed at low temperature for YAgTe$_2$ (Fig. 8(f)) and YCuTe$_2$ (Fig. 8(i)) suggesting low-frequency phonon modes and hence, low thermal conductivity. To investigate the influence of London dispersion forces to the thermal properties, the heat capacity of YAgTe$_2$ was calculated with and without inclusion of van der Waals forces. The computed heat capacity including van der Waals forces among the layers show an enhanced correlation with experiments in the intermediate temperature range (Fig. 8(e)). At low temperature, the inclusion of dispersion forces underestimated the heat capacity due to an overestimation of the forces, whereas without dispersion forces the computed heat capacity is overestimated (Fig. 8(f)). However, the discrepancy between computation and experiments is small and within uncertainty of the calculation. A slight overestimation was observed for YCuTe$_2$ without inclusion of dispersion forces (Fig. 8(i)). Note that the electronic contributions to the heat capacity ($\gamma_{\mathrm{el,YAgTe_2}} \sim 0.7$ mJ mol^{-1} K^{-2} and $\gamma_{\mathrm{el,YCuTe_2}} \sim 0.5$ mJ mol^{-1} K^{-2}), deduced by fitting the experimental heat capacity, were added to the computed heat capacity.

In addition to the phonon dispersion curves, the partial phonon DOS of the investigated XYZ_2 compounds were recorded and compared to Raman spectra. The partial phonon DOS indicates that Te and Ag atoms (in TmAgTe$_2$ and YAgTe$_2$) are responsible for low-frequency optical phonon modes which might suppress the acoustic modes (Fig. 7(a) and (b)). Slightly higher phonon frequencies of the acoustic modes were calculated for YCuTe$_2$. Furthermore, both compounds containing Ag and Te exhibit a large split of the longitudinal and transverse acoustic modes along Γ and Z directions. Thus, lower thermal conductivity is predicted for TmAgTe$_2$ and YAgTe$_2$ compared to YCuTe$_2$. While the phonon DOS of the Ag-based compounds peak at 40 cm^{-1} and 110 cm^{-1}, the phonon DOS of YCuTe$_2$ peaks at 70 cm^{-1} and 120 cm^{-1}. The phonon frequencies are consistent with the Raman spectra where YCuTe$_2$ has slightly higher frequencies than the Ag-based compounds as well a small peak can be observed experimentally around 70 cm^{-1} for Y$_{0.96}$Cu$_{1.08}$Te$_2$ (Fig. S14†). However, the Raman spectra were not calculated from the phonon dispersion curves and a quantitative comparison concerning the accuracy of the phonon dispersion curves at the Brillouin zone center cannot be provided.

The thermal conductivities of the investigated XYZ_2 compounds were measured as a function of temperature from 2 K up to 850 K (Fig. 9). All compounds exhibit extremely low thermal conductivity over the entire temperature range. The thermal conductivities increased with temperature up to around 50 K ($\sim$110 K for TmAgTe$_2$), followed by a decrease in thermal conductivity, likely due to phonon–phonon interactions. The HT-phase of TmAgTe$_2$ and the extrinsically doped compounds have similar thermal conductivities whereas the thermal conductivity of the LT-phase is nearly twice that of the HT-phase (Fig. 9(a)). This finding is consistent with the heat capacity, which was higher for the tetragonal phase than the trigonal phase (Fig. 8(a)). Above 700 K, an increase in thermal conductivity was measured for TmAgTe$_2$, suggesting a bipolar contribution to the thermal conductivity. However, the electronic contribution of the thermal conductivity generally increases with temperature. To determine the phonon contribution to the thermal conductivity, the electronic contribution to the thermal conductivity was calculated with the Wiedemann–Franz law ($\kappa_e = L_{\mathrm{eff}}T/\rho$) where the effective Lorenz number, L_{eff}, was determined from the experimental Seebeck coefficients using the single-parabolic band model (SPB).[80] The SPB model assumes that electron scattering is limited by acoustic phonon. To delineate the origins of the increase in thermal conductivity of TmAgTe$_2$ at high temperature, the electronic contribution thus was calculated and subtracted. The resulting phonon contribution of the thermal conductivity increased slightly at high temperature, but within the uncertainty. The phonon contributions of all investigated XYZ_2 compounds decreased with temperature, suggesting that phonon–phonon interactions are the limiting scattering factor. The lowest thermal conductivity was measured for the HT-phase of TmAgTe$_2$ and the corresponding extrinsically doped compounds ($\kappa_p = 0.26 \pm 0.04$ W m^{-1} K^{-1} above 700 K), enhancing the thermoelectric performance. Similar low thermal conductivity was reported for Ag$_2$Te, which dips as low as 0.14 W m^{-1} K^{-1}, suggesting that the combination of Ag and Te results in a low thermal conductivity.[81] However, the LT-phase of TmAgTe$_2$ ($\kappa_p = 0.47 \pm 0.07$ W m^{-1} K^{-1} at 625 K) and YAgTe$_2$ ($\kappa_p = 0.36 \pm 0.05$ W m^{-1} K^{-1} at 725 K) both exhibited higher phonon thermal conductivity than the trigonal phase of TmAgTe$_2$ indicating that the crystal structure plays a significant role in thermal conductivity. The lattice thermal conductivity of YCuTe$_2$ ($\kappa_p = 0.39 \pm 0.06$ W m^{-1} K^{-1} at 800 K) was the highest for all investigated parent compounds, which agrees well with the computed phonon dispersion curves (Fig. 7).

To investigate the lowest limit of the thermal conductivity, the minimum thermal conductivity models of Cahill and Pohl[38,39] and Pöhls et al.[20,40] were applied. The latter approach can be separated in static disordering (i.e., disordering of the atoms in the crystal lattice) and dynamic disordering (i.e., disordering through phonon–phonon interactions). While the static approach reached the minimum thermal conductivity already at low temperature (<300 K), dynamic disordering requires high temperature as the thermal conductivity decreases with T^{-1}.

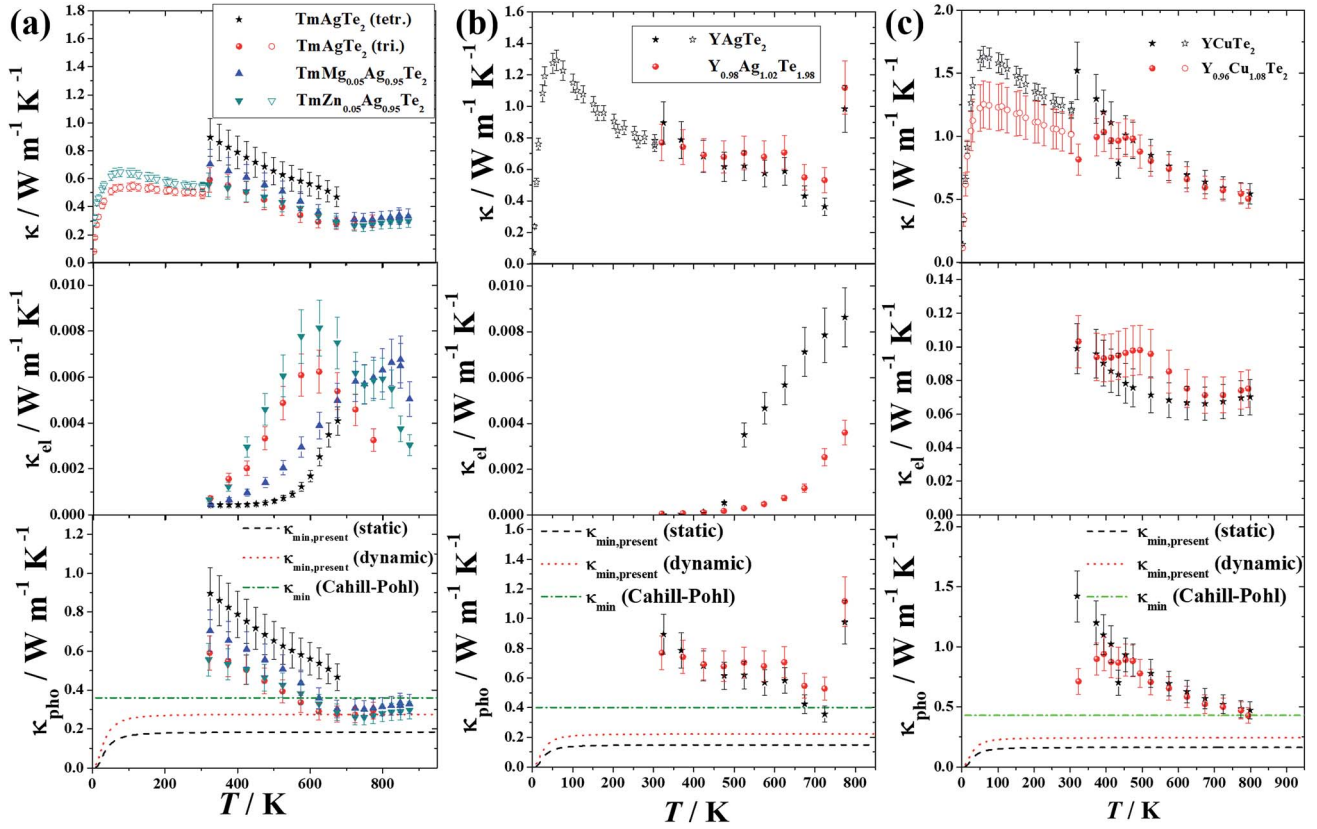**Fig. 9** Total thermal conductivity, electronic and phononic contribution of (a) TmAgTe$_2$, (b) YAgTe$_2$, and (c) YCuTe$_2$ (including the corresponding doped compounds). The thermal conductivity of all parent compounds decreased below the Cahill and Pohl[38,39] minimum thermal conductivity limit (κ_{min}). The experimental thermal conductivity of HT-TmAgTe$_2$ approaches the dynamic limit (*i.e.*, phonon mean free path is frequency-dependent) whereas the static limit (*i.e.*, phonon mean free path is frequency-independent) underestimates the thermal conductivity. High-temperature thermal conductivity of the LT- and HT-phase of TmAgTe$_2$ was taken from ref. 22 and the high-temperature thermal conductivity of YCuTe$_2$ and Y$_{0.96}$Cu$_{1.08}$Te$_2$ was taken from ref. 23.

The lattice thermal conductivity of TmAgTe$_2$ compounds in the trigonal phase are all below the minimum thermal conductivity described by the model of Cahill and Pohl.[38,39] The thermal conductivity of TmAgTe$_2$ approached the minimum thermal conductivity limited by dynamic disordering above 700 K and remained at that value to ~840 K. The phonon contributions to the thermal conductivity of YAgTe$_2$ and YCuTe$_2$ are already below the amorphous limit and the temperature trend suggests that the phonon contribution decreases further with temperature. Thus, the minimum thermal conductivity limited by dynamic disordering might better represent the lowest limit of thermal conductivity than the amorphous limit (Cahill–Pohl) model. All investigated *XYZ*$_2$ compounds exhibit lower lattice thermal conductivity than 0.5 W m^{-1} K^{-1}, which had been assumed as the phonon contribution of the thermal conductivity in the previous study by Zhu *et al.*[22] and therefore are even more promising than expected as thermoelectric materials.

3.4. Thermoelectric figure of merit

The thermoelectric figure of merit, *zT*, was calculated using eqn (1) from polynomial fits of the experimental electronic and thermal data. The *zT* values of all compounds (Fig. 10) studied

increase with temperature and the highest *zT* was found in Y$_{0.96}$Cu$_{1.08}$Te$_2$ (0.73 ± 0.18 at 780 K), as reported semi-quantitatively in our previous study.[23] The experimental
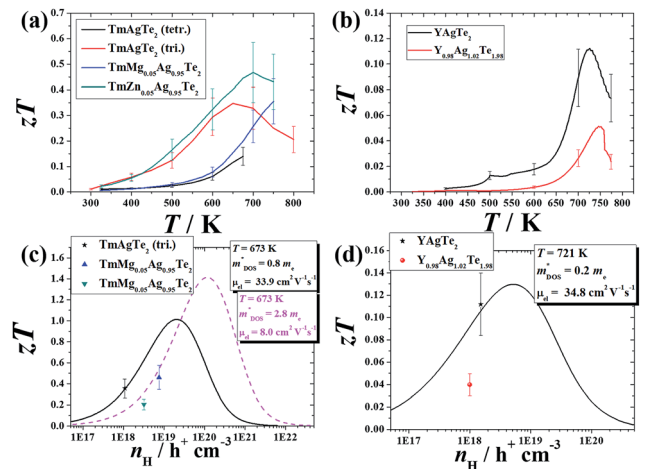

Fig. 10 Experimental thermoelectric figure of merit, *zT*, and SPB model of (a, b) TmAgTe$_2$ and (c, d) YAgTe$_2$. The *zT* of the Zn-doped TmAgTe$_2$ compound increased by ~35% compared to the previous reported HT-phase parent compound.[22]

performance was compared with the computed properties at 600 K with the lattice thermal conductivity setting to the amorphous limit.[38,39] The experimental thermoelectric performance of YCuTe$_2$ has a strong correlation with the predicted zT (Table S8†). Especially when SOC is included, the calculated zT is within expected uncertainty of the experimental value in the HT-phase. The computed thermoelectric performance of the LT-phase is lower than the HT-phase, most likely due to the reduced band gap energy (Table S3†).

In this study, the thermoelectric performance of TmAgTe$_2$ increased nearly 35% by doping the Ag-site with Zn ($zT \sim 0.47 \pm 0.12$ at 700 K) compared to HT-phase in the previous study ($zT \sim 0.35 \pm 0.09$ at 650 K).[22] While zT of the HT-phase and Zn-doped sample peaked below 750 K, zT for the LT-phase and the Mg-doped was still increasing even at the highest measurement temperature. Due to the irreversible phase transformation, the LT-phase of TmAgTe$_2$ was measured only to 675 K and a relatively low zT was reported.[22] The Mg-doped sample might be a promising candidate for high-temperature thermoelectrics as the zT is already at 0.35 ± 0.09 at 750 K and the temperature trend suggests further increase. Whereas the computed zT of LT-TmAgTe$_2$ is within uncertainty of the experimental value at 600 K, the computed zT of the HT-TmAgTe$_2$ is half the experimental zT (Table S9†). The lower predicted thermoelectric performance of HT-TmAgTe$_2$ can be explained by an overestimation of the lattice thermal conductivity using the amorphous limit model of Cahill–Pohl. It has to be noted that a shorter relaxation time was assumed for TmAgTe$_2$ than for the other investigated compounds and thus, information of the exact relaxation time is required to enhance the prediction of the thermoelectric properties.

Both YAgTe$_2$ compounds exhibited relatively low zTs with a peak around 750 K, followed by a decrease at the HT-phase. The lower zTs of TmAgTe$_2$ and YAgTe$_2$ can be a result of the low carrier concentration and thus, the optimized carrier concentration was calculated using the SPB model, indicating that the zT of YAgTe$_2$ could be only slightly increased with enhanced carrier concentration (Fig. 10(d)). The zT of TmAgTe$_2$, on the other hand, can in theory be dramatically increased to ~ 1.0 by doping the compound to a carrier concentration of $\sim 3 \times 10^{19}$ cm^{-3} (Fig. 10(b)). However, the zT values of the extrinsically doped compounds do not agree with the SPB model. A higher DOS effective mass, m^*_{DOS}, was calculated for the extrinsically doped samples. The value of m^*_{DOS} increased from 0.8 m_e for the HT-phase to 2.8 m_e for the Zn-doped compound, which might be due to two factors: increase in carrier concentration and change in DOS with extrinsic doping. A change in the experimental DOS was observed with Mg-doping, which does not show the same feature at the Fermi energy as the parent compound (Fig. 3). The experimental DOS suggests that the thermoelectric performance of Mg-doped TmAgTe$_2$ would be reduced at low temperatures and a dramatic increase in performance would be expected at high temperature, as confirmed experimentally (Fig. 10(a)). Note that the DOS of the Zn-doped compound cannot be investigated due to the high vapor pressure of Zn. The effect of the carrier concentration on the effective mass was calculated using BoltzTraP, as described

by Ricci et al.[70] The conductivity effective mass nearly doubles if the carrier concentration is increased from 2.5×10^{18} cm^{-3} to 2.5×10^{19} cm^{-3} (Table S10†). The increase in conductive mass can be attributed to the additional bands, which contribute to the electrical properties when the Fermi level falls deeper in the valence region. With a higher m^*_{DOS} and a lower mobility, the SPB predicts that zT can increase to 1.4 with an optimized carrier concentration of $\sim 10^{20}$ cm^{-3}. These results encourage further doping studies of TmAgTe$_2$ in combination with computational study to enhance the thermoelectric performance.

4. Conclusions

In the present study, the physical and thermoelectric properties of three XYZ_2 compounds, TmAgTe$_2$, YAgTe$_2$, and YCuTe$_2$, were investigated to evaluate the accuracy of the prediction of the thermoelectric properties using semi-classical Boltzmann transport equations. Since all studied compounds crystallize in a layered structure at low temperature, van der Waals interactions were included for the LT-phases of YAgTe$_2$ and TmAgTe$_2$, and a better prediction of the interlayered distance was observed. The compounds in the trigonal phase, however, have larger interlayered distance and charged ions between the layers and thus van der Waals interactions were negligible. The influence of van der Waals interactions on the thermal properties is expected: the neglect of van der Waals interactions results in an underestimation of the interlayered forces and hence an overestimation of the heat capacity at low temperature. Interestingly, a split of the nearly degenerate bands at the VBM is observed with the inclusion of van der Waals interactions, which is similar to the band structures calculated with SOC due to different shifts in the bond energy and hence, the degeneracy left of the bands. However, while SOC split the degenerate Te–Tm–Ag bands, the increase in interatomic forces with the inclusion of DFT-D3 increased the split in bonding and anti-bonding orbitals and hence, pushed the anti-bonding orbitals of Te–Ag in the band gap of Te–Tm–Ag bands. Thus, inclusion of van der Waals is not only important because it can provide better lattice parameters, but also because it can enhance the electronic band structure prediction. If both methods, DFT-D3 and SOC, were included, the degeneracy at the VBM increased compared to each individual method. Further investigations of the effect of van der Waals interactions on the electronic band structures are required. The electrical conductivity was calculated from the calculated band structures and a temperature-dependent relaxation time limited by acoustic phonons, showing good agreement with experiments over the entire temperature range. While at low temperature the accurate prediction of the bands shapes (by including SOC and DFT-D3) leads to a better agreement with the experimental electronic properties, intrinsic (bipolar) effects can contribute significantly at high temperatures. However, the HSE06 electronic band structure does not improve the prediction of the band gap energy because the PBE-GGA band gap energy is more than five times higher than the thermal energy.

In addition to the comparison of the computed thermoelectric properties with experiments, a significant increase of zT in TmAgTe$_2$ was observed with Zn-doping on the Ag-site due to an increase in hole carrier concentration. Further enhancement of the thermoelectric performance of TmAgTe$_2$ is predicted with optimization of the hole carrier concentration.

Acknowledgements

Notes and references

1 C. Ravi and C. Wolverton, *Acta Mater.*, 2004, **52**, 4213–4227.
2 S. M. Woodley and R. Catlow, *Nat. Mater.*, 2008, 7, 937–946.
3 M. Gajdoš, K. Hummer, G. Kresse, J. Furthmüller and F. Bechstedt, *Phys. Rev. B: Condens. Matter Mater. Phys.*, 2006, **73**, 045112.
4 G. Y. Guo, K. C. Chu, D.-s. Wang and C.-g. Duan, *Phys. Rev. B: Condens. Matter Mater. Phys.*, 2004, **69**, 205416.
5 J. J. Palacios, A. J. Pérez-Jiménez, E. Louis, E. SanFabián and J. A. Vergés, *Phys. Rev. B: Condens. Matter Mater. Phys.*, 2002, **66**, 035322.
6 X. Li, J. T. Mullen, Z. Jin, K. M. Borysenko, M. B. Nardelli and K. W. Kim, *Phys. Rev. B: Condens. Matter Mater. Phys.*, 2013, **87**, 115418.
7 D. A. Broido, M. Malorny, G. Birner, N. Mingo and D. A. Stewart, *Appl. Phys. Lett.*, 2007, **91**, 231922.
8 J. Garg, N. Bonini, B. Kozinsky and N. Marzari, *Phys. Rev. Lett.*, 2011, **106**, 045901.
9 J. M. Cole, K. S. Low, H. Ozoe, P. Stathi, C. Kitamura, H. Kurata, P. Rudolf and T. Kawase, *Phys. Chem. Chem. Phys.*, 2014, **16**, 26684–26690.
10 Q. Yan, G. Li, P. F. Newhouse, J. Yu, K. A. Persson, J. M. Gregoire and J. B. Neaton, *Adv. Energy Mater.*, 2015, **5**, 1401840.
11 G. Ceder, *MRS Bull.*, 2010, **35**, 693–701.
12 A. Urban, D.-H. Seo and G. Ceder, *npj Comput. Mater.*, 2016, **2**, 16002.
13 H. Chen, Q. Hao, O. Zivkovic, G. Hautier, L.-S. Du, Y. Tang, Y.-Y. Hu, X. Ma, C. P. Grey and G. Ceder, *Chem. Mater.*, 2013, **8**, 2777–2786.
14 X. Meng, Z. Liu, B. Cui, D. Qin, H. Geng, W. Cai, L. Fu, J. He, Z. Ren and J. Sui, *Adv. Energy Mater.*, 2017, **7**, 1602582.
15 J. Carrete, N. Mingo, S. Wang and S. Curtarolo, *Adv. Funct. Mater.*, 2014, **24**, 7427–7432.
16 J. He, M. Amsler, Y. Xia, S. S. Naghavi, V. I. Hegde, S. Hao, S. Goedecker, V. Ozoliņ and C. Wolverton, *Phys. Rev. Lett.*, 2016, **117**, 046602.
17 P. Gorai, E. S. Toberer and V. Stevanovic, *Phys. Chem. Chem. Phys.*, 2016, **18**, 31777–31786.
18 L. Bjerg, G. K. H. Madsen and B. B. Iversen, *Chem. Mater.*, 2011, **23**, 3907–3914.
19 G. K. H. Madsen, *J. Am. Chem. Soc.*, 2006, **128**, 12141–12146.
20 J.-H. Pöhls, A. Faghaninia, G. Petretto, U. Aydemir, F. Ricci, G. Li, M. Wood, S. Ohno, G. Hautier, G. J. Snyder, G.-M. Rignanese, A. Jain and M. A. White, *J. Mater. Chem. C*, 2017, **5**, 12441–12456.
21 A. Jain, S. P. Ong, G. Hautier, W. Chen, W. D. Richards, S. Dacek, S. Cholia, D. Gunter, D. Skinner, G. Ceder and K. A. Persson, *APL Mater.*, 2013, **1**, 011002.
22 H. Zhu, G. Hautier, U. Aydemir, Z. M. Gibbs, G. Li, S. Bajaj, J.-H. Pöhls, D. Broberg, W. Chen, A. Jain, M. A. White, M. Asta, G. J. Snyder, K. Persson and G. Ceder, *J. Mater. Chem. C*, 2015, **3**, 10554–10565.
23 U. Aydemir, J.-H. Pöhls, H. Zhu, G. Hautier, S. Bajaj, Z. M. Gibbs, W. Chen, G. Li, S. Ohno, D. Broberg, S. D. Kang, M. Asta, G. Ceder, M. A. White, K. Persson, A. Jain and G. J. Snyder, *J. Mater. Chem. A*, 2016, **4**, 2461–2472.
24 H. Lin, H. Chen, J.-N. Shen, L. Chen and L.-M. Wu, *Chem.–Eur. J.*, 2014, **20**, 15401–15408.
25 W. Chen, J.-H. Pöhls, G. Hautier, D. Broberg, S. Bajaj, U. Aydemir, Z. M. Gibbs, H. Zhu, M. Asta, G. J. Snyder, B. Meredig, M. A. White, K. Persson and A. Jain, *J. Mater. Chem. C*, 2016, **4**, 4414–4426.
26 J. Heyd, J. E. Peralta and G. E. Scuseria, *J. Chem. Phys.*, 2005, **123**, 174101.
27 A. J. Garza and G. E. Scuseria, *J. Phys. Chem. Lett.*, 2016, **7**, 4165–4170.
28 M. Chan and G. Ceder, *Phys. Rev. Lett.*, 2010, **105**, 196403.
29 W. Setyawan, R. M. Gaume, S. Lam, R. S. Feigelson and S. Curtarolo, *ACS Comb. Sci.*, 2011, **13**, 382–390.
30 F. Dybała, M. P. Polak, J. Kopaczek, P. Scharoch, K. Wu, S. Tongay and R. Kudrawiec, *Sci. Rep.*, 2016, **6**, 26663.
31 M. Aykol, S. Kim and C. Wolverton, *J. Phys. Chem. C*, 2015, **119**, 19053–19058.
32 B. Van Troeye, M. Torrent and X. Gonze, arXiv:1801.08741v1 [cond-mat.mtrl-sci], 2018.
33 X. Luo, M. B. Sullivan and S. Y. Quek, *Phys. Rev. B: Condens. Matter Mater. Phys.*, 2012, **86**, 184111.
34 S. J. Kim, S. Hu, C. Uher and M. G. Kanatzidis, *Chem. Mater.*, 1999, **11**, 3154–3159.

35 J. L. Lan, Y. C. Liu, B. Zhan, Y. H. Lin, B. Zhang, X. Yuan, W. Zhang, W. Xu and C. W. Nan, *Adv. Mater.*, 2013, **25**, 5086–5090.

36 N. V. Nong, N. Pryds, S. Linderoth and M. Ohtaki, *Adv. Mater.*, 2011, **23**, 2484–2490.

37 M. J. van Setten, M. Giantomassi, X. Gonze, G.-M. Rignanese and G. Hautier, *Phys. Rev. B: Condens. Matter Mater. Phys.*, 2017, **96**, 155207.

38 D. G. Cahill and R. O. Pohl, *Annu. Rev. Phys. Chem.*, 1988, **39**, 93–121.

39 D. G. Cahill, S. K. Watson and R. O. Pohl, *Phys. Rev. B: Condens. Matter Mater. Phys.*, 1992, **46**, 6131–6140.

40 J.-H. Pöhls, M. B. Johnson and M. A. White, *Phys. Chem. Chem. Phys.*, 2016, **18**, 1185–1190.

41 G. Kresse and J. Furthmüller, *Phys. Rev. B: Condens. Matter Mater. Phys.*, 1996, **54**, 11169–11186.

42 J. P. Perdew, K. Burke and M. Ernzerhof, *Phys. Rev. Lett.*, 1996, **77**, 3865–3868.

43 G. Kresse and D. Joubert, *Phys. Rev. B: Condens. Matter Mater. Phys.*, 1999, **59**, 1758–1775.

44 J. Heyd, G. E. Scuseria and M. Ernzerhof, *J. Chem. Phys.*, 2003, **118**, 8207–8215.

45 J. Paier, M. Marsman, K. Hummer, G. Kresse, I. C. Gerber and J. G. Angyán, *J. Chem. Phys.*, 2006, **124**, 154709.

46 S. Grimme, J. Antony, S. Ehrlich and S. Krieg, *J. Chem. Phys.*, 2010, **132**, 154104.

47 G. K. H. Madsen and D. J. Singh, *Comput. Phys. Commun.*, 2006, **175**, 67–71.

48 A. Kokalj, *Comput. Mater. Sci.*, 2003, **28**, 155–168.

49 A. Togo and I. Tanaka, *Scr. Mater.*, 2015, **108**, 1–5.

50 A. Togo, L. Chaput, I. Tanaka and G. Hug, *Phys. Rev. B: Condens. Matter Mater. Phys.*, 2010, **81**, 174301.

51 C. A. Kennedy, M. Stancescu, R. A. Marriott and M. A. White, *Cryogenics*, 2007, **47**, 107–112.

52 D. G. Archer, *J. Phys. Chem. Ref. Data*, 1993, **22**, 1441–1453.

53 B. Saparov, F. Hong, J.-P. Sun, H.-S. Duan, W. Meng, S. Cameron, I. G. Hill, Y. Yan and D. B. Mitzi, *Chem. Mater.*, 2015, **27**, 5622–5632.

54 K. A. Borup, E. S. Toberer, L. D. Zoltan, G. Nakatsukasa, M. Errico, J. P. Fleurial, B. B. Iversen and G. J. Snyder, *Rev. Sci. Instrum.*, 2002, **83**, 123902.

55 S. Iwanaga, E. S. Toberer, A. LaLonde and G. J. Snyder, *Rev. Sci. Instrum.*, 2011, **82**, 063905.

56 O. Maldonado, *Cryogenics*, 1992, **32**, 908–912.

57 C. A. Kennedy and M. A. White, *Solid State Commun.*, 2005, **134**, 271–276.

58 C. Delmas, C. Fouassie and P. Hagenmuller, *Physica B+C*, 1980, **99**, 81–85.

59 R. D. Shannon, *Acta Crystallogr., Sect. A: Cryst. Phys., Diffr., Theor. Gen. Crystallogr.*, 1976, **32**, 751–767.

60 L. Gulay, J. Stępièn-Damm, M. Daszkiewicz and A. Pietraszko, *J. Alloys Compd.*, 2007, **431**, L1–L3.

61 M.-P. Pardo, M. Julien-Pouzol and M. J. Flahaut, *Comptes Rendus Hebdomadaires des Seances de l'Academie des Sciences*, 1973, **276**, 599–602.

62 L. Gulay, I. Olekseyuk and A. Pietraszko, *J. Alloys Compd.*, 2006, **424**, 159–163.

63 F. Ortmann, F. Bechstedt and W. G. Schmidt, *Phys. Rev. B: Condens. Matter Mater. Phys.*, 2006, **72**, 205101.

64 A. O. de-la Roza and E. R. Johnson, *J. Chem. Phys.*, 2012, **136**, 174109.

65 A. D. Becke and E. R. Johnson, *J. Chem. Phys.*, 2007, **127**, 154108.

66 A. D. Becke and E. R. Johnson, *J. Chem. Phys.*, 2007, **127**, 124108.

67 S.-D. Guo, *J. Alloys Compd.*, 2016, **663**, 128–133.

68 T. J. Scheidemantel, C. Ambrosch-Draxl, T. Thonhauser, J. V. Badding and J. O. Sofo, *Phys. Rev. B: Condens. Matter Mater. Phys.*, 2003, **68**, 125120.

69 X. Peng, Q. Wei and A. Copple, *Phys. Rev. B: Condens. Matter Mater. Phys.*, 2014, **90**, 085402.

70 F. Ricci, W. Chen, U. Aydemir, G. J. Snyder, G.-M. Rignanese, A. Jain and G. Hautier, *Sci. Data*, 2017, **4**, 170085.

71 E. S. Toberer, P. Rauwel, S. Gariel, J. Taftø and G. J. Snyder, *J. Mater. Chem.*, 2010, **20**, 9877–9885.

72 H. Xie, H. Wang, Y. Pei, C. Fu, X. Liu, G. J. Snyder, X. Zhao and T. Zhu, *Adv. Funct. Mater.*, 2013, **23**, 5123–5130.

73 B. Wölfing, C. Kloc, J. Teubner and E. Bucher, *Phys. Rev. Lett.*, 2001, **86**, 4350–4353.

74 Z. M. Gibbs, H.-S. Kim, H. Wang and G. J. Snyder, *Appl. Phys. Lett.*, 2015, **106**, 022112.

75 A. Seko, A. Togo, H. Hayashi, K. Tsuda, L. Chaput and I. Tanaka, *Phys. Rev. Lett.*, 2015, **115**, 205901.

76 M. de Jong, W. Chen, T. Angsten, A. Jain, R. Notestine, A. Gamst, M. Sluiter, C. K. Ande, S. van der Zwaag, J. J. Plata, C. Toher, S. Curtarolo, G. Ceder, K. A. Persson and M. Asta, *Sci. Data*, 2015, **2**, 150009.

77 V. V. Novikov, N. A. Zhemoedov, N. V. Mitroshenkov and A. V. Matovnikov, *Dalton Trans.*, 2016, **45**, 17447–17452.

78 J. P. C. Ruff, J. P. Clancy, A. Bourque, M. A. White, M. Ramazanoglu, J. S. Gardner, Y. Qiu, J. R. D. Copley, M. B. Johnson, H. A. Dabkowska and B. D. Gaulin, *Phys. Rev. Lett.*, 2008, **101**, 147205.

79 J. F. Niven, M. B. Johnson, A. Bourque, P. J. Murray, D. D. James, H. A. Dąbkowska, B. D. Gaulin and M. A. White, *Proc. R. Soc. A*, 2014, **470**, 0140387.

80 A. F. May, E. S. Toberer, A. Saramat and G. J. Snyder, *Phys. Rev. B: Condens. Matter Mater. Phys.*, 2009, **80**, 125205.

81 Y. Pei, N. A. Heinz and G. J. Snyder, *J. Mater. Chem.*, 2011, **21**, 18256–18260.